UNIVERSIDAD NACIONAL AUTÓNOMA DE MÉXICO
POSGRADO EN CIENCIAS FÍSICAS

OPTICAL RESPONSE OF PARTIALLY EMBEDDED NANOSPHERES

TESIS
QUE PARA OPTAR POR EL GRADO DE:
MAESTRO EN CIENCIAS (FÍSICA)

PRESENTA:

JONATHAN ALEXIS URRUTIA ANGUIANO

TUTOR:

DR. ALEJANDRO REYES CORONADO
FACULTAD DE CIENCIAS, UNAM

MIEMBROS DEL COMITÉ TUTOR

DRA. CITLALI SÁNCHEZ-AKÉ
INSTITUTO DE CIENCIAS APLICADAS Y TECNOLOGÍA, UNAM

DR. GIUSEPPE PIRRUCCIO
INSTITUTO DE FÍSICA, UNAM

CIUDAD DE MÉXICO, MÉXICO, 2022

Abstract/Resumen

Lorem ipsum dolor sit amet, consectetuer adipiscing elit. Etiam lobortis facilisis sem. Nullam nec mi et neque pharetra sollicitudin. Praesent imperdiet mi nec ante. Donec ullamcorper, felis non sodales commodo, lectus velit ultrices augue, a dignissim nibh lectus placerat pede. Vivamus nunc nunc, molestie ut, ultricies vel, semper in, velit. Ut porttitor. Praesent in sapien. Lorem ipsum dolor sit amet, consectetuer adipiscing elit. Duis fringilla tristique neque. Sed interdum libero ut metus. Pellentesque placerat. Nam rutrum augue a leo. Morbi sed elit sit amet ante lobortis sollicitudin. Praesent blandit blandit mauris. Praesent lectus tellus, aliquet aliquam, luctus a, egestas a, turpis. Mauris lacinia lorem sit amet ipsum. Nunc quis urna dictum turpis accumsan semper.

Contents

Background and Motivation

It is recommended to fill in this part of the document with the following information:

Metasurfaces are bidimensaional arrays of unit cells with geometrical dimensions smaller than the wavelength of the incident light. Biosensing-aimed metasurfaces are supported onto a substrate and immersed in an aqueous medium, thus its performance is limited by its washability. One alternative to decrease a metasurface's washability is to partially embed it within the substrate while allowing the metasurface to still interact with the aqueous medium. In this work, we study the optical response of a single partially embedded metallic nanosphere and extend its behavior analytically into a disordered metasurface by employing an effective medium approach.

The incrustation of the metasurface is studied by calculating the spectral behavior of a single partially embedded nanosphere with the Finite Element Method (FEM) and proposing an effective polarizability in the elements of the metasurface.

- Your field: Context about the field your are working
  Plasmonics -> Metameterials -> Biosensing

- Motivation: Backgroung about your thesis work and why did you choose this project and why is it important.
  Fabrication -> Partially embedded NPs -> No analytical (approximated) method physically introduces the incrustation degree. There are numerical solutions and Effective Medium Theories approaching the problem but the later only as a fitting method.

- Objectives: What question are you answering with your work.
  Can optical non invasive tests (IR-Vis) retrieve the average incrustation degree for monolayers of small spherical particles?

- Methology: What are your secondary goals so you achieve your objective. Also, how are you answering yout question: which method or model.
  Bruggeman homogenization theories on bidimensional systems?
  Is the dipolar approximation is enough or do we need more multipolar terms?
  Do we need the depolarization factors?

- Structure: How is this thesis divides and what is the content of each chapter.

Scattering Theory of a Single Spherical Particle

The problem addressed in this thesis corresponds to the numerical analysis of the Localized Surface Plasmon Resonances (LSPR) excited on plasmonic spherical nanoparticles (NPs) when these are under realistic experimental conditions, such as those present on plasmonic biosensors, where the NPs are partially embedded into a substrate [1]. The performed analysis consists on the numerical calculation of the absorption, scattering and extinction cross sections of a partially embedded metal NP, employing the Finite Element Method (FEM) . To verify the validity of the obtained results, the problem of the absorption and scattering of light by a single spherical particle is addressed. In this chapter, we revisit the general solution of the light absorption and scattering by both an arbitrary particle and a spherical particle, given by the Mie Theory[1] [4].

1.1 The Optical Theorem: Amplitude Matrix and Cross Sections

Let $\mathbf{E}^{\mathrm{i}} = \mathbf{E}_0^{\mathrm{i}} \exp(i\mathbf{k}^{\mathrm{i}} \cdot \mathbf{r})$ be the electric field of an incident monochromatic plane wave with constant amplitude $\mathbf{E}_0^{\mathrm{i}}$ traveling through a non absorbing medium with refractive index n_{mat}, denominated as the matrix, in the direction $\mathbf{k}^{\mathrm{i}} = k\hat{\mathbf{k}}^{\mathrm{i}}$, with $k = (\omega/c)n_{\mathrm{mat}}$ the wave number of the plane wave into the matrix, and let $\mathbf{E}^{\mathrm{sca}}$ be the scattered electric field due to a particle with arbitrary shape embedded into the matrix. In general, the scattered electric field propagates in all directions but for an observation point $\mathbf{r} = r\hat{\mathbf{e}}_r$, the traveling direction is defined by the vector $\mathbf{k}^{\mathrm{sca}} = k\hat{\mathbf{k}}^{\mathrm{sca}} = k\hat{\mathbf{e}}_r$. Due to the linearity of the Maxwell's equations, the incident and scattered electric fields in the far field regime are related by the following linear relation [5]:

$$\mathbf{E}^{\mathrm{sca}} = \frac{\exp(i\mathbf{k}^{\mathrm{sca}} \cdot \mathbf{r})}{r}\mathbb{F}(\hat{\mathbf{k}}^{\mathrm{sca}}, \hat{\mathbf{k}}^{\mathrm{i}})\mathbf{E}^{\mathrm{i}}, \qquad (1.1)$$

---

[1]The term *Mie Theory* refers rather to a solution set to Maxwell's equations for the scattering of a electromagnetic plane wave due to a spherical particle, developed by Gustav Mie and published on 1907 [2]. Ludving Lorenz published beforehand an equivalent solution to the same scattering problem nevertheless, Mie's solution consists in an iterative method suited for easier computations, which boosted its spread [3].

where $\mathbb{F}(\hat{\mathbf{k}}^{\mathrm{sca}}, \hat{\mathbf{k}}^{\mathrm{i}})$ is the scattering amplitude matrix from direction $\hat{\mathbf{k}}^{\mathrm{i}}$ into $\hat{\mathbf{k}}^{\mathrm{sca}}$. Since only the far field is considered, both the incident and the scattered electric fields can be decomposed into two linearly independent components perpendicular to $\mathbf{k}^{\mathrm{i}}$ and $\mathbf{k}^{\mathrm{sca}}$, respectively, each forming a right-handed orthonormal system. If the particle acting as a scatterer has a symmetric shape, it is convenient to define an orthonormal system relative to the scattering plane, which is the plane containing $\mathbf{k}^{\mathrm{i}}$ and $\mathbf{k}^{\mathrm{sca}}$ since the elements of $\mathbb{F}(\hat{\mathbf{k}}^{\mathrm{sca}}, \hat{\mathbf{k}}^{\mathrm{i}})$ get simplified when represented in these bases [5]. In Fig. 1.1 a plane wave traveling in the z direction illuminates an arbitraty particle centered at the origin of the coordinated system and the scatterig plane is depicted in green. By defining the directions perpendicular ($\perp$) and parallel ($\parallel$) to the scattering plane, the incident and scattered electric fields can be written as

$$\mathbf{E}^{\mathrm{i}} = \left(E^{\mathrm{i}}_{\parallel} \hat{\mathbf{e}}^{\mathrm{i}}_{\parallel} + E^{\mathrm{i}}_{\perp} \hat{\mathbf{e}}^{\mathrm{i}}_{\perp} \right) \exp\left(i\mathbf{k}^{\mathrm{i}} \cdot \mathbf{r} \right), \tag{1.2}$$

$$\mathbf{E}^{\mathrm{sca}} = \left(E^{\mathrm{sca}}_{\parallel} \hat{\mathbf{e}}^{\mathrm{sca}}_{\parallel} + E^{\mathrm{sca}}_{\perp} \hat{\mathbf{e}}^{\mathrm{sca}}_{\perp} \right) \frac{\exp(i\mathbf{k}^{\mathrm{sca}} \cdot \mathbf{r})}{r}, \tag{1.3}$$

where a harmonic time dependence $\exp(-i\omega t)$ has been omitted, and where it has been assumed that the scattered field is described by a spherical wave; the superindex 'i' ('sca') denotes the orthonormal system defined by the incident plane wave (scattered fields). Since $\{\hat{\mathbf{e}}^{\mathrm{i}}_{\perp}, \hat{\mathbf{e}}^{\mathrm{i}}_{\parallel}, \hat{\mathbf{k}}^{\mathrm{i}}\}$ and $\{\hat{\mathbf{e}}^{\mathrm{sca}}_{\perp}, \hat{\mathbf{e}}^{\mathrm{sca}}_{\parallel}, \hat{\mathbf{k}}^{\mathrm{sca}}\}$ —shown in purple in Fig. 1.1 along with the Cartesian (blue) and spherical (black) unit vector bases— are right-handed orthonormal systems, they are related as follows

$$\hat{\mathbf{e}}^{\mathrm{i}}_{\perp} = \hat{\mathbf{e}}^{\mathrm{sca}}_{\perp} = \hat{\mathbf{k}}^{\mathrm{sca}} \times \hat{\mathbf{k}}^{\mathrm{i}}, \qquad \hat{\mathbf{e}}^{\mathrm{i}}_{\parallel} = \hat{\mathbf{k}}^{\mathrm{i}} \times \hat{\mathbf{e}}^{\mathrm{i}}_{\perp}, \qquad \text{and} \qquad \hat{\mathbf{e}}^{\mathrm{sca}}_{\parallel} = \hat{\mathbf{k}}^{\mathrm{sca}} \times \hat{\mathbf{e}}^{\mathrm{sca}}_{\perp}. \tag{1.4}$$
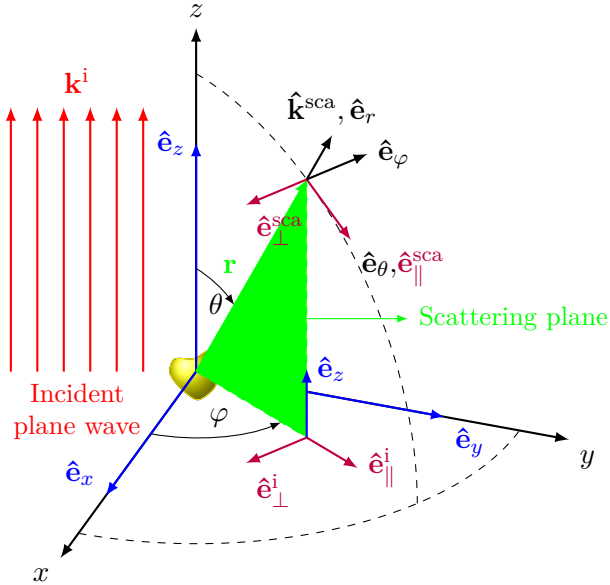

Fig. 1.1: The scattering plane (green) is defined by the vectors $\hat{\mathbf{k}}^{\mathrm{i}}$ (red) —the direction of the incident plane wave— and $\hat{\mathbf{k}}^{\mathrm{sca}}$ —the direction of the scattered field in a given point $\vec{r}$—. If the direction of the incident plane wave is chose to be $\hat{\mathbf{e}}_z$, then the parallel and perpendicular components of the incident field relative to the scattering plane are $\hat{\mathbf{e}}^{\mathrm{i}}_{\parallel} = \cos\varphi\, \hat{\mathbf{e}}_x + \sin\varphi\, \hat{\mathbf{e}}_y$ and $\hat{\mathbf{e}}^{\mathrm{i}}_{\perp} = -\hat{\mathbf{e}}_\varphi$, while the components of the scattering field relative to the scattering plane are $\hat{\mathbf{e}}^{\mathrm{sca}}_{\parallel} = \hat{\mathbf{e}}_\theta$, $\hat{\mathbf{e}}^{\mathrm{sca}}_{\perp} = -\hat{\mathbf{e}}_\varphi$. The Cartesian unit vector basis is shown in blue, the spherical unit vector basis in black, while the basis of the orthonormal systems relative to the scattering plane are shown in purple.

As the Eqs. (1.4) suggest, the unit vector bases of the orthonormal systems relative to the scattering plane depend on the scattering direction. For example, if the incident plane wave travels along the z axis (Fig. 1.1), then $\hat{\mathbf{k}}^{\mathrm{i}} = \hat{\mathbf{e}}_z$ and $\hat{\mathbf{k}}^{\mathrm{sca}} = \hat{\mathbf{e}}_r$. Thus the unit vector bases of the systems relative to the scatterig plane are $\hat{\mathbf{e}}_\parallel^{\mathrm{i}} = \cos\varphi\,\hat{\mathbf{e}}_x + \sin\varphi\,\hat{\mathbf{e}}_y$, $\hat{\mathbf{e}}_\parallel^{\mathrm{sca}} = \hat{\mathbf{e}}_\theta$ and $\hat{\mathbf{e}}_\perp^{\mathrm{i}} = \hat{\mathbf{e}}_\perp^{\mathrm{sca}} = -\hat{\mathbf{e}}_\varphi$, with θ the polar angle and φ azimuthal angle.

When an incident plane wave interacts with a particle with a complex refractive index $n_{\mathrm{p}}(\omega)$, the total electric field outside the particle is given by the sum of the incident and the scattered fields. Therefore, the time averaged Poynting vector $\langle\mathbf{S}\rangle_t$, denoting the power flow per unit area, of the total field is given by

$$\langle\mathbf{S}\rangle_t = \underbrace{\frac{1}{2}\operatorname{Re}\left(\mathbf{E}^{\mathrm{i}}\times\mathbf{H}^{\mathrm{i}*}\right)}_{\langle\mathbf{S}^{\mathrm{i}}\rangle_t} + \underbrace{\frac{1}{2}\operatorname{Re}\left(\mathbf{E}^{\mathrm{sca}}\times\mathbf{H}^{\mathrm{sca}*}\right)}_{\langle\mathbf{S}^{\mathrm{sca}}\rangle_t} + \underbrace{\frac{1}{2}\operatorname{Re}\left(\mathbf{E}^{\mathrm{i}}\times\mathbf{H}^{\mathrm{sca}*} + \mathbf{E}^{\mathrm{sca}}\times\mathbf{H}^{\mathrm{i}*}\right)}_{\langle\mathbf{S}^{\mathrm{ext}}\rangle_t}, \qquad (1.5)$$

where $(*)$ is the complex conjugate operation and where the total Poynting vector is separated in three terms: the contribution from the incident field $\langle\mathbf{S}^{\mathrm{i}}\rangle_t$, from the scattered field $\langle\mathbf{S}^{\mathrm{sca}}\rangle_t$ and from their cross product denoted by $\langle\mathbf{S}^{\mathrm{ext}}\rangle_t$. By means of the Faraday-Lenz law and Eq. (1.1), the contribution to the Poynting vector from the incident and the scattered fields can be rewritten as

$$\left\langle\mathbf{S}^{\mathrm{i}}\right\rangle_t = \frac{\|\mathbf{E}_0^{\mathrm{i}}\|^2}{2Z_{\mathrm{mat}}}\hat{\mathbf{k}}^{\mathrm{i}}, \qquad \text{and} \qquad \langle\mathbf{S}^{\mathrm{sca}}\rangle_t = \frac{\|\mathbf{E}^{\mathrm{sca}}\|^2}{2Z_{\mathrm{mat}}}\hat{\mathbf{k}}^{\mathrm{sca}} = \frac{\left\|\mathbb{F}(\hat{\mathbf{k}}^{\mathrm{sca}},\hat{\mathbf{k}}^{\mathrm{i}})\mathbf{E}^{\mathrm{i}}\right\|^2}{2Z_{\mathrm{mat}}r^2}\hat{\mathbf{k}}^{\mathrm{sca}}, \qquad (1.6)$$

with $Z_{\mathrm{mat}} = \sqrt{\mu_{\mathrm{mat}}/\varepsilon_{\mathrm{mat}}}$, the impedance of the non-absorbing matrix, while the crossed contribution is given by

$$\begin{aligned}\left\langle\mathbf{S}^{\mathrm{ext}}\right\rangle_t = \operatorname{Re}\Bigg\{ &\frac{\exp\left[-i(\mathbf{k}^{\mathrm{sca}}-\mathbf{k}^{\mathrm{i}})\cdot\mathbf{r}\right]}{2Z_{\mathrm{mat}}r^2}\left[\hat{\mathbf{k}}^{\mathrm{sca}}\left(\mathbf{E}_0^{\mathrm{i}}\cdot\mathbb{F}^*\mathbf{E}^{\mathrm{i}*}\right) - \mathbb{F}^*\mathbf{E}^{\mathrm{i}*}\left(\mathbf{E}_0^{\mathrm{i}}\cdot\hat{\mathbf{k}}^{\mathrm{sca}}\right)\right] \\ &+\frac{\exp\left[i(\mathbf{k}^{\mathrm{sca}}-\mathbf{k}^{\mathrm{i}})\cdot\mathbf{r}\right]}{2Z_{\mathrm{mat}}r^2}\left[\hat{\mathbf{k}}^{\mathrm{i}}\left(\mathbb{F}\mathbf{E}^{\mathrm{i}}\cdot\mathbf{E}_0^{\mathrm{i}*}\right) - \mathbf{E}_0^{\mathrm{i}*}\left(\mathbb{F}\mathbf{E}^{\mathrm{i}}\cdot\hat{\mathbf{k}}^{\mathrm{i}}\right)\right]\Bigg\}, \end{aligned} \qquad (1.7)$$

where the scattering amplitude matrix is evaluated as $\mathbb{F}(\hat{\mathbf{k}}^{\mathrm{sca}},\hat{\mathbf{k}}^{\mathrm{i}})$.

The power scattered by the particle can be calculated by integrating $\langle\mathbf{S}^{\mathrm{sca}}\rangle_t$ in a closed surface surrounding the particle; if the scattered power is normalized by the irradiance of the incident field $\|\langle\mathbf{S}^{\mathrm{i}}\rangle_t\|$, it is obtained a quantity with units of area, known as the scattering cross section C_{sca}, given by [4]

Scattering Cross Section

$$C_{\mathrm{sca}} = \frac{2Z_{\mathrm{mat}}}{\|\mathbf{E}_0\|^2}\oint_{\mathbb{S}}\langle\mathbf{S}^{\mathrm{sca}}\rangle_t\cdot\mathrm{d}\mathbf{a} = \oint_{\mathbb{S}}\frac{\left\|\mathbb{F}(\hat{\mathbf{k}}^{\mathrm{sca}},\hat{\mathbf{k}}^{\mathrm{i}})\mathbf{E}^{\mathrm{i}}\right\|^2}{\|\mathbf{E}_0^{\mathrm{i}}\|^2}\,\mathrm{d}\Omega\,, \qquad (1.8)$$

where $\mathrm{d}\Omega$ is the differential solid angle.

Similarly, an absorption cross section C_{abs} can be defined as well. On the one side, the absorption cross section is given by the integral on a closed surface of $(1-)\langle \mathbf{S} \rangle_t$ [Eq. (1.5)] divided by the irradiance of the incident field, where the minus sign is chosen so that $C_{\text{abs}} > 0$ if the particle absorbs energy [4]. On the other side, if an Ohmic material for the particle with conductivity $\sigma(\omega) = i\omega n_{\text{p}}^2(\omega)$ [6] is assumed, through Joule's heating law [5] the absorption cross section can be computed as

Ohmic Particle - Absorption Cross Section

$$C_{\text{abs}} = \frac{1}{2} \int_{\mathcal{V}} \frac{\text{Re}(\mathbf{J} \cdot \mathbf{E}^{\text{int}*})}{\|\mathbf{E}_0^{\text{i}}\|^2 / 2Z_{\text{mat}}} \, dV = \int_{\mathcal{V}} \omega Z_{\text{mat}} \, \text{Im}(n_{\text{p}}^2) \frac{\|\mathbf{E}^{\text{int}}\|^2}{\|\mathbf{E}_0^{\text{i}}\|^2} \, dV \,, \qquad (1.9)$$

where integration is performed inside the particle, and $\mathbf{J}$ and $\mathbf{E}^{\text{int}}$, are the volumetric electric current density and the total electric field in this region, respectively. Both the scattering and the absorption cross sections are quantities related to the optical signature of a particle [7], and their relation can be made explicit by performing the surface integral representation of C_{abs} and defining C_{ext}, that is,

$$\begin{aligned}
C_{\text{abs}} &= -\frac{2Z_{\text{mat}}}{\|\mathbf{E}_0^{\text{i}}\|^2} \int_{\mathbb{S}} \left(\left\langle \mathbf{S}^{\text{i}} \right\rangle_t + \langle \mathbf{S}^{\text{sca}} \rangle_t + \left\langle \mathbf{S}^{\text{ext}} \right\rangle_t \right) \cdot d\mathbf{a} \\
&= -C_{\text{sca}} - \frac{2Z_{\text{mat}}}{\|\mathbf{E}_0^{\text{i}}\|^2} \int_{\mathbb{S}} \left\langle \mathbf{S}^{\text{ext}} \right\rangle_t \cdot \hat{\mathbf{e}}_r \, d\Omega \\
&= -C_{\text{sca}} + C_{\text{ext}},
\end{aligned} \qquad (1.10)$$

where the contribution of $\langle \mathbf{S}^{\text{i}} \rangle_t$ to the integral is zero since a non-absorbing matrix was assumed. From Eq.(1.10) it can be seen that C_{ext} takes into account both mechanisms for energy losses (scattering and absorption), thus it is called the extinction cross section. To solve the integral in Eq. (1.10) let us define θ as the angle between $\hat{\mathbf{k}}^{\text{sca}}$ and $\hat{\mathbf{k}}^{\text{i}}$ as the polar angle and φ as the azimuthal angle, as shown in Fig 1.1. With this choice of coordinates, the extinction cross section can be computed as

$$\begin{aligned}
C_{\text{ext}} = -\text{Re}\Bigg\{ &\frac{\exp(-ikr)}{\|\mathbf{E}_0^{\text{i}}\|^2} \oint_{\mathbb{S}} \exp(ikr\cos\theta)(1)\Big(\mathbf{E}^{\text{i}} \cdot \mathbb{F}^* \mathbf{E}^{\text{i}*}\Big) \, d\Omega \\
&+ \frac{\exp(ikr)}{\|\mathbf{E}_0^{\text{i}}\|^2} \oint_{\mathbb{S}} \exp(-ikr\cos\theta)\cos\theta\Big(\mathbf{E}^{\text{i}*} \cdot \mathbb{F}\mathbf{E}^{\text{i}}\Big) \, d\Omega \\
&+ \frac{\exp(ikr)}{\|\mathbf{E}_0^{\text{i}}\|^2} \oint_{\mathbb{S}} \exp(-ikr\cos\theta)\sin\theta(E_{0,x}^{\text{i}}\cos\varphi + E_{0,y}^{\text{i}}\sin\varphi)\Big(\mathbb{F}\mathbf{E}^{\text{i}} \cdot \mathbf{k}^{\text{i}}\Big) \, d\Omega \Bigg\},
\end{aligned} \qquad (1.11)$$

using that $\hat{\mathbf{k}}^{\text{sca}} \cdot \hat{\mathbf{e}}_r = 1$, $\hat{\mathbf{k}}^{\text{i}} \cdot \hat{\mathbf{e}}_r = \cos\theta$ and $\mathbf{E}^{\text{sca}} \cdot \hat{\mathbf{e}}_r = 0$. The integrals in Eq. (1.11) can be solved by a two-fold integration by parts in the polar angle θ and by neglecting terms proportional to r^{-2}. This process leads to a zero contribution from the integrand proportional to $\sin\theta$ in Eq. (1.11) and, after rearranging the other terms in their real and imaginary parts, it follows that C_{ext} depends only on the forward direction $\hat{\mathbf{k}}^{\text{sca}} = \hat{\mathbf{k}}^{\text{i}}$ ($\theta = 0$). This result is known as the Optical Theorem whose mathematical expression is given by [5, 7, 8]:

> **Optical Theorem - Extinction Cross Section**
>
> $$C_{\text{ext}} = C_{\text{abs}} + C_{\text{sca}} = \frac{4\pi}{k\|\mathbf{E}_0^{\text{i}}\|^2} \, \text{Im} \left[\mathbf{E}_0^{\text{i}} \cdot \mathbb{F}^*(\hat{\mathbf{k}}^{\text{i}}, \hat{\mathbf{k}}^{\text{i}}) \mathbf{E}^{\text{i}*} \right]. \tag{1.12}$$

The Optical Theorem is a general result applicable to general scattering phenomena, both quantum and classical [4, 8] and its derivation rely in the incident field being a plane wave [see Eq. (1.11)] and more precisely, in the lack of longitudinal components of the incident field [9, 10].

From Eqs. (1.5) and (1.12) it can be seen that the extinction of light, the combined result of scattering and absorption as energy loss mechanisms, is also a manifestation of the interference between the incident and the scattered fields and, remarkably, that the overall effect of the light extinction can be fully understood by analyzing the amplitude of the scattering field in the forward direction. It is worth noting that Eq. (1.12) is an exact relation but its usefulness is bond to the correct evaluation of the scattering amplitude matrix $\mathbb{F}$ [5]. Thus, in the following Sections a scattering problem with spherical symmetry will be assumed, so that the exact solution to the scattering amplitude matrix can be developed; this solution is known as the *Mie Theory*.

1.2   Mie Scattering

In the previous Section, it was concluded that the extinction of light due to the interaction between a particle and a monochromatic plane wave can be determined through the amplitude of the scattered field in the forward direction. This is stated in the Optical Theorem, which is an exact relation, but inaccuracies may arise when either the scattering amplitude matrix or the extinction cross section are approximated[2]. A particular case in which the scattering amplitude matrix can be exactly calculated is when the scatterer has spherical symmetry. In order to address this special case, it will be introduced a vectorial basis with spherical symmetry, known as the Vector Spherical Harmonics (VSH). Once the VSH are defined, they will be used to write a monochromatic plane wave in terms of the VSH. By imposing the continuity of the tangential components of the electric and magnetic fields, the scattered field can be also written in terms of the VSH. As a particular example of interest, in the last Section, the optical properties of a gold nanoparticle with radius of 12.5 nm are calculated.

1.2.1   Vector Spherical Harmonics

The electric and magnetic fields, denoted as **E** and **B**, respectively, corresponds to a solution to the homogeneous vectorial Helmholtz when a harmonic time dependence and a spatial domain with no external charge nor current densities is assumed, that is,

---

[2]See for example Section 2.4 from Ref. [5] on the Rayleigh Scattering and Section 21.7 from Ref. [11] on Thompson scattering.

Vectorial Helmholtz Equation

$$\boldsymbol{\nabla}^2 \mathbf{E}(\mathbf{r}, \omega) + k^2 \mathbf{E}(\mathbf{r}, \omega) = \mathbf{0}, \qquad \boldsymbol{\nabla}^2 \mathbf{B}(\mathbf{r}, \omega) + k^2 \mathbf{B}(\mathbf{r}, \omega) = \mathbf{0}. \qquad (1.13)$$

where the vectorial operator $\boldsymbol{\nabla}^2$ must be understood as $\boldsymbol{\nabla}^2 = \nabla(\nabla\cdot) - \nabla \times \nabla\times$, and k is the wave number in the matrix, which follows the dispersion relation $k = (\omega/c)n_{\mathrm{mat}}$, with $n_{\mathrm{mat}} = \sqrt{\mu_{\mathrm{mat}}\varepsilon_{\mathrm{mat}}/\mu_0\varepsilon_0}$ the refractive index of the matrix, μ_{mat} its magnetic permeability and $\varepsilon_{\mathrm{mat}}$ its dielectric function. It is possible to build a basis set for the electric and magnetic fields as long as the elements of this basis are also solution to Eq. (1.13). One alternative is to employ the following set of vector functions [12]

$$\mathbf{L} = \nabla\psi, \tag{1.14a}$$

$$\mathbf{M} = \nabla \times (\mathbf{r}\psi), \tag{1.14b}$$

$$\mathbf{N} = \frac{1}{k}\nabla \times \mathbf{M}, \tag{1.14c}$$

that are solution to the homogeneous vectorial Helmholtz equation as long as the scalar function ψ is solution to the scalar Helmholtz equation[3]

$$\nabla^2\psi + k^2\psi = 0. \tag{1.15}$$

The triad $\{\mathbf{L}, \mathbf{M}, \mathbf{N}\}$ is a set of vectors[4]that obey Helmholtz equation *i.e.*, they can be directly identified as electric or magnetic fields. The elements of the vector basis from Eq. (1.14) are known as the Vector Spherical Harmonics and are defined as Stratton [12], or by Bohren and Huffman [4], and the scalar function ψ is known as the generating function of the VSH. From the definition of the VSH in Eqs. (1.14) it can be seen that $\mathbf{L}$ has only a longitudinal component, while $\mathbf{M}$ has only transversal components —specifically $\mathbf{M}$ is tangential to any sphere of radius $\|\mathbf{r}\|$—, and $\mathbf{N}$ have both longitudinal and transversal components.

If spherical coordinates are chosen, and it is assumed that $\psi(r,\theta,\varphi) = R(r)\Theta(\theta)\Phi(\varphi)$, then Eq. (1.15) can be decoupled into three ordinary differential equations:

$$\frac{\mathrm{d}^2\Phi}{\mathrm{d}\varphi^2} + m^2\Phi = 0, \tag{1.16}$$

$$\frac{1}{\sin\theta}\frac{\mathrm{d}}{\mathrm{d}\theta}\left(\sin\theta\frac{\mathrm{d}\Theta}{\mathrm{d}\theta}\right) + \left[\ell(\ell+1) - \frac{m^2}{\sin^2\theta}\right]\Theta = 0, \tag{1.17}$$

$$\frac{\mathrm{d}}{\mathrm{d}r}\left(r^2\frac{\mathrm{d}R}{\mathrm{d}r}\right) + \left[(kr)^2 - \ell(\ell+1)\right]R = 0, \tag{1.18}$$

where ℓ takes natural values and zero, and $|m| \leq \ell$ so tha Φ and Θ are univalued and finite on a

---

[3]This result can be proved by considering the following: Let f be $\mathcal{C}^3$ and $\mathbf{F}$ a $\mathcal{C}^2$. Then, it is true that $\nabla^2(\nabla f) = \nabla(\nabla^2 f)$, and $\boldsymbol{\nabla} \times \left(\boldsymbol{\nabla}^2\mathbf{F}\right) = \boldsymbol{\nabla}^2(\boldsymbol{\nabla} \times \mathbf{F})$.

[4]Using the Einstein sum convention with ϵ_{ijk} the Levi-Civita symbol, Eq. (1.14b) can be written as follows: $M_i = [\nabla \times (\mathbf{r}\psi)]_i = \epsilon_{ijk}\partial_j(r_k\psi) = \psi\epsilon_{ijk}\partial_j(r_k) - \epsilon_{ikj}r_k\partial_j\psi = \psi[\nabla \times \mathbf{r}]_i - [\mathbf{r} \times \nabla\psi]_i = -[\mathbf{r} \times \nabla\psi]_i = [\mathbf{L} \times \mathbf{r}]_i$,therefore $\mathbf{M}$ is orthogonal to $\mathbf{L}$ and $\mathbf{r}$. From Eq. (1.14c) $\mathbf{M} \cdot \mathbf{N} = 0$, so $\mathbf{M}$ is orthogonal to $\mathbf{N}$. As it will be shown in Eq. (1.22), not necessarily $\mathbf{L}$ is orthogonal to $\mathbf{N}$ in a geometrical sense.

sphere. The Eqs. (1.17) and (1.18) can be rewritten as

$$(1 - \mu^2)\frac{\mathrm{d}^2\Theta}{\mathrm{d}\mu^2} - 2\mu\frac{\mathrm{d}\Theta}{\mathrm{d}\mu} + \left[\ell(\ell+1) - \frac{m^2}{1-\mu^2}\right]\Theta = 0, \quad \text{with } \mu = \cos\theta, \tag{1.19}$$

$$\rho\frac{\mathrm{d}}{\mathrm{d}\rho}\left(\rho\frac{\mathrm{d}Z}{\mathrm{d}\rho}\right) + \left[\rho^2 - \left(\ell + \frac{1}{2}\right)^2\right]Z = 0, \quad \text{with } Z = R\sqrt{\rho} \text{ and } \rho = kr. \tag{1.20}$$

The solution to Eq. (1.19) are the associated Legendre functions $P_\ell^m(\mu)$ and to Eq. (1.20) the solution is given by the spherical Bessel functions of the first (j_ℓ) and second (y_ℓ) kind, or the spherical Hankel functions of first ($h_\ell^{(1)} = j_\ell + iy_\ell$) and second ($h_\ell^{(2)} = j_\ell - iy_\ell$) kind. Following the convention from most Mie Scattering literature [11], the solution to Eq. (1.16) will be decompose into an odd ('o') and an even ('e') solution, that is, as sine and cosine functions, thus restricting the values of m to non negative integers. After this procedure, it is determined that the generating function of the VSH is given by

ψ: Generating function of the vectorial spherical harmonics

$$\psi_{\substack{\mathrm{e}\\\mathrm{o}}\ell m}(r,\theta,\varphi) = \frac{\sin(m\varphi)}{\cos(m\varphi)}P_\ell^m(\cos\theta)z_\ell(kr). \tag{1.21}$$

where z_ℓ stands for any of the four solutions to the radial equation [Eq. (1.20)]. Substituting Eq. (1.21) in Eqs. (1.14a)–(1.14c) one finds the even VSH

Vectorial Spherical Harmonics

$$\mathbf{L}_{\substack{\mathrm{e}\\\mathrm{o}}m\ell} = \frac{\cos(m\varphi)}{\sin(m\varphi)}kP_\ell^m(\cos\theta)\frac{\mathrm{d}z_\ell(kr)}{\mathrm{d}(kr)}\,\hat{\mathbf{e}}_r + \frac{\cos(m\varphi)}{\sin(m\varphi)}k\frac{z_\ell(kr)}{kr}\frac{\mathrm{d}P_\ell^m(\cos\theta)}{\mathrm{d}\theta}\,\hat{\mathbf{e}}_\theta +$$

$$\frac{-\sin(m\varphi)}{+\cos(m\varphi)}km\frac{P_\ell^m(\cos\theta)}{\sin\theta}\frac{z_\ell(kr)}{kr}\,\hat{\mathbf{e}}_\varphi \tag{1.22a}$$

$$\mathbf{M}_{\substack{\mathrm{e}\\\mathrm{o}}m\ell} = \frac{-\sin(m\varphi)}{+\cos(m\varphi)}mz_\ell(kr)\frac{P_\ell^m(\cos\theta)}{\sin\theta}\,\hat{\mathbf{e}}_\theta - \frac{\cos(m\varphi)}{\sin(m\varphi)}z_\ell(kr)\frac{\mathrm{d}P_\ell^m(\cos\theta)}{\mathrm{d}\theta}\,\hat{\mathbf{e}}_\varphi, \tag{1.22b}$$

$$\mathbf{N}_{\substack{\mathrm{e}\\\mathrm{o}}m\ell} = \frac{\cos(m\varphi)}{\sin(m\varphi)}\frac{z_\ell(kr)}{kr}\ell(\ell+1)P_\ell^m(\cos\theta)\,\hat{\mathbf{e}}_r + \frac{\cos(m\varphi)}{\sin(m\varphi)}\frac{1}{kr}\frac{\mathrm{d}[kr\,z_\ell(kr)]}{\mathrm{d}(kr)}\frac{\mathrm{d}P_\ell^m(\cos\theta)}{\mathrm{d}\theta}\,\hat{\mathbf{e}}_\theta +$$

$$\frac{-\sin(m\varphi)}{+\cos(m\varphi)}m\frac{1}{kr}\frac{\mathrm{d}[kr\,z_\ell(kr)]}{\mathrm{d}(kr)}\frac{P_\ell^m(\cos\theta)}{\sin\theta}\,\hat{\mathbf{e}}_\varphi, \tag{1.22c}$$

where the term $\ell(\ell+1)P_\ell^m$ arises since the associated Legendre functions obeys Eq. (1.19).

The choice at z_ℓ in Eqs. (1.22) is due to the physical constraints of the scattering problem. On one hand, the spherical Bessel function of first kind, unlike the other three proposed solutions to the radial equation, is finite at $r = 0$, thus it is appropriate for the internal electric field and plane waves. This choice at z_ℓ will be denoted in the VSH with the superscript (1). On the other hand, the asymptotic behavior ($\ell \ll \rho$) of the Hankel function of first kind $h^{(1)} = j_\ell + iy_\ell$ and its

derivative are outgoing spherical waves [4]

$$h_\ell^{(1)}(\rho) \approx (-i)^\ell \frac{\exp(i\rho)}{i\rho} \quad \text{and} \quad \frac{\mathrm{d}h_\ell^{(1)}(\rho)}{\mathrm{d}\rho} \approx (-i)^\ell \frac{\exp(i\rho)}{\rho}, \tag{1.23}$$

which are suited for the scattered field; the VSH with $z_\ell = h_\ell^{(1)}$ will be denoted with the superscript (3).

From here on, the VSH will be those defined in Eq. (1.14) under the condition of being a solution to the vectorial Helmholtz equation, which lead to the generating function ψ to be a solution to the scalar Helmholtz equation. Nevertheless, there are other definitions for the VSH as discussed by Barrera, Estevez, and Giraldo [13]. The chosen definition of the VSH allows the VSH to be interpreted directly as electric and magnetic fields, specifically identifying $\mathbf{N}$ with the electric contribution and $\mathbf{M}$ with the magnetic due to its behavior in the far field regime[5], as it will be shown in the Section 1.2.3.1.

1.2.2 Incident, Scattered, and Internal Electric Fields

Let $\mathbf{E}^{\mathrm{i}}$ be a x-polarized plane wave traveling in the $\mathbf{e}_z$ direction; its representation in the spherical unit vector basis is

$$\mathbf{E}^{\mathrm{i}}(\mathbf{r}) = E_0(\sin\theta\cos\varphi\,\hat{\mathbf{e}}_r + \cos\theta\cos\varphi\,\hat{\mathbf{e}}_\theta - \sin\varphi\,\hat{\mathbf{e}}_\varphi)\exp(ikr\cos\theta). \tag{1.24}$$

The monochromatic plane wave is a transversal wave, thus it can be written in terms of only the VSH $\mathbf{M}^{(1)}$ and $\mathbf{N}^{(1)}$, where the radial dependency is given by j_ℓ since the monochromatic plane wave is finite everywhere. Even more, due to the dependence on φ, it is only restricted to values of $m = 1$. By inspection on the radial component of $\mathbf{E}^{\mathrm{i}}$, proportional to $\cos\varphi$, it depends only on $\mathbf{N}_{e1\ell}^{(1)}$, and on the azimuthal component, proportional to $\sin\varphi$, it depends only on $\mathbf{M}_{o1\ell}^{(1)}$. Thus, Eq. (1.24) can be written as the linear combination of $\mathbf{N}_{e1\ell}^{(1)}$ and $\mathbf{M}_{o1\ell}^{(1)}$. Through the orthogonality relations of the VSH [see Eqs. (A.22)–(A.25) from Appendix A], the x-polarized plane wave can be written as [12]

$$\mathbf{E}^{\mathrm{i}}(\mathbf{r}) = E_0 \sum_\ell \frac{i^\ell(2\ell+1)}{\ell(\ell+1)}\Big(\mathbf{M}_{o1\ell}^{(1)} - i\mathbf{N}_{e1\ell}^{(1)}\Big), \tag{1.25a}$$

$$\mathbf{H}^{\mathrm{i}}(\mathbf{r}) = \frac{-kE_0}{\mu\omega} \sum_\ell \frac{i^\ell(2\ell+1)}{\ell(\ell+1)}\Big(\mathbf{M}_{e1\ell}^{(1)} + i\mathbf{N}_{o1\ell}^{(1)}\Big), \tag{1.25b}$$

where the sum over the index ℓ is done for integer values larger or equal to one.

In the problem of scattering due to a spherical particle of radius a, the continuity conditions

---

[5]The VSH $\mathbf{L}$ is left out from the identification of either an electric or magnetic contribution since it is purely longitudinal and thus is neglected in the far field.

on the tangential components of the electric and magnetic fields are written as

$$\left(\mathbf{E}^{\mathrm{i}} + \mathbf{E}^{\mathrm{sca}} - \mathbf{E}^{\mathrm{int}}\right)\Big|_{r=a} \times \hat{\mathbf{e}}_r = \left(\mathbf{H}^{\mathrm{i}} + \mathbf{H}^{\mathrm{sca}} - \mathbf{H}^{\mathrm{int}}\right)\Big|_{r=a} \times \hat{\mathbf{e}}_r = 0, \tag{1.26}$$

with $\mathbf{E}^{\mathrm{sca}}$ ($\mathbf{E}^{\mathrm{int}}$) the scattered (internal) electric field and $\mathbf{H}^{\mathrm{sca}}$ ($\mathbf{H}^{\mathrm{int}}$) the scattered (internal) magnetic field. If the incident field $\mathbf{E}^{\mathrm{i}}$ is given by a x-polarized plane wave [Eq. (1.24)] then the scattered and internal fields can be written also as a linear combination of $\mathbf{M}_{o1\ell}$ and $\mathbf{N}_{e1\ell}$. The internal field is finite inside the particle, thus the radial dependency is given by the function $j_\ell(k_{\mathrm{p}}a)$, with k_{p} the wave number inside the particle. For the scattered fields, it is chosen the spherical Hankel function of first kind $h^{(1)}(ka)$ due to its asymptotic behavior of a spherical outgoing wave. Such choice for the radial dependency is denoted by the superscript (3) over the VSH. To simplify the following steps, the scattered and the internal electric fields are proposed as

$$\mathbf{E}^{\mathrm{sca}}(\mathbf{r}) = E_0 \sum_\ell \frac{i^\ell(2\ell+1)}{\ell(\ell+1)}\left(ia_\ell\mathbf{N}_{e1\ell}^{(3)} - b_\ell\mathbf{M}_{o1\ell}^{(3)}\right), \tag{1.27a}$$

$$\mathbf{E}^{\mathrm{int}}(\mathbf{r}) = E_0 \sum_\ell \frac{i^\ell(2\ell+1)}{\ell(\ell+1)}\left(c_\ell\mathbf{M}_{o1\ell}^{(1)} - id_\ell\mathbf{N}_{e1\ell}^{(1)}\right), \tag{1.27b}$$

with the respective magnetic fields

$$\mathbf{H}^{\mathrm{sca}}(\mathbf{r}) = \frac{-kE_0}{\mu\omega} \sum_\ell \frac{i^\ell(2\ell+1)}{\ell(\ell+1)}\left(ib_\ell\mathbf{N}_{o1\ell}^{(3)} + a_\ell\mathbf{M}_{e1\ell}^{(3)}\right), \tag{1.28a}$$

$$\mathbf{H}^{\mathrm{int}}(\mathbf{r}) = \frac{-kE_0}{\mu_{\mathrm{p}}\omega} \sum_\ell \frac{i^\ell(2\ell+1)}{\ell(\ell+1)}\left(d_\ell\mathbf{M}_{e1\ell}^{(1)} + ic_\ell\mathbf{N}_{o1\ell}^{(1)}\right). \tag{1.28b}$$

Since only the term $m = 1$ is taken into account, it is convenient to define the angular functions

$$\pi_\ell(\cos\theta) = \frac{P_\ell^1(\cos\theta)}{\sin\theta}, \quad \text{and} \quad \tau_\ell(\cos\theta) = \frac{\mathrm{d}P_\ell^1(\cos\theta)}{\mathrm{d}\theta}, \tag{1.29}$$

which are not orthogonal but their addition and substraction are, that is $\pi_\ell \pm \tau_\ell$ are orthogonal functions [4]; see Eq. (A.20) in Appendix A. After substitution of Eqs. (1.25), (1.27) and (1.28) into Eq. (1.26) and considering the orthogonality between $\mathbf{M}$ and $\mathbf{N}$, between even and odd VSH , and between $\pi_\ell \pm \tau_\ell$, it is shown that the coefficients a_ℓ, b_ℓ, c_ℓ and d_ℓ are given by two decoupled equation systems

$$\begin{pmatrix} [xh_\ell^{(1)}(x)] & (\mu/\mu_{\mathrm{p}})[(mx)j_\ell(mx)] \\ m[xh_\ell^{(1)}(x)]' & [(mx)j_\ell(mx)]' \end{pmatrix} \begin{pmatrix} a_\ell \\ d_\ell \end{pmatrix} = \begin{pmatrix} [xj_\ell(x)] \\ m[xj_\ell(x)]' \end{pmatrix}, \tag{1.30}$$

and

$$\begin{pmatrix} m[xh_\ell^{(1)}(x)] & [(mx)j_\ell(mx)] \\ [xh_\ell^{(1)}(x)]' & (\mu/\mu_{\mathrm{p}})[(mx)j_\ell(mx)]' \end{pmatrix} \begin{pmatrix} b_\ell \\ c_\ell \end{pmatrix} = \begin{pmatrix} m[xj_\ell(x)] \\ [xj_\ell(x)]' \end{pmatrix}, \tag{1.31}$$

where $m = k_{\mathrm{p}}/k = n_{\mathrm{p}}/n_{\mathrm{mat}}$ is the contrast between the sphere and the matrix, $x = ka = 2\pi n_{\mathrm{mat}}(a/\lambda)$ is the size parameter and ($'$) denotes the derivative respect to the argument of the

spherical Bessel or Hankel functions; the size parameter compares the size of the scatterer to the incident wavelength in the matrix: the larger the value of x, the bigger the scatterer can be considered inside such matrix. The Eqs. (1.30) and (1.31) are simplified when the Riccati-Bessel functions $\psi_\ell(\rho) = \rho j_\ell(\rho)$ and $\xi(\rho) = \rho h_\ell^{(1)}(\rho)$ are introduced.

When a non-magnetic particle nor matrix are assumed ($\mu_{\mathrm{p}} = \mu = \mu_0$), the coefficients a_ℓ and b_ℓ are known as the Mie coefficients, whose expression is calculated by inverting Eqs. (1.30) and (1.31), yielding

Mie Coefficients

$$a_\ell = \frac{\psi_\ell(x)\psi_\ell'(mx) - m\psi_\ell(mx)\psi_\ell'(x)}{\xi_\ell(x)\psi_\ell'(mx) - m\psi_\ell(mx)\xi_\ell'(x)}, \tag{1.32a}$$

$$b_\ell = \frac{m\psi_\ell(x)\psi_\ell'(mx) - \psi_\ell(mx)\psi_\ell'(x)}{m\xi_\ell(x)\psi_\ell'(mx) - \psi_\ell(mx)\xi_\ell'(x)}. \tag{1.32b}$$

Likewise, the coefficients c_ℓ and d_ℓ are given by

$$c_\ell = \frac{-m\xi_\ell'(x)\psi_\ell(x) + m\xi_\ell(x)\psi_\ell'(x)}{m\xi_\ell(x)\psi_\ell'(mx) - \psi_\ell(mx)\xi_\ell'(x)}, \tag{1.33a}$$

$$d_\ell = \frac{-m\xi_\ell'(x)\psi_\ell(x) + m\psi_\ell'(mx)\psi_\ell'(x)}{\xi_\ell(x)\psi_\ell'(mx) - m\psi_\ell(mx)\xi_\ell'(x)}. \tag{1.33b}$$

Even though the coefficients of the linear combination for the scattered and internal fields were obtained assuming an x-polarized incident field, due to the spherical symmetry of the problem, by applying the transformation $\varphi \to \varphi + \pi/2$ the same procedure is valid for a y-polarized incident field [4], therefore all quantities related to the scattered and the internal field can be expressed in terms of Eqs. (1.32) and (1.33).

As discussed in Section 1.1, the optical properties of a particle are encoded into the scattering, absorption and extinction cross sections. These quantities can be calculated by means of the scattering amplitude matrix [Eq. (1.1)] and the Optical Theorem [Eq. (1.12)]. Since the particle is spherical, it is convinient to exploit the symmetry of the problem by decomposing the scattered electric field [Eq. (1.27a)] into components parallel and perpendicular to the scattering plane. To obtain the scattering amplitude matrix expressed in an orthogonal base relative to the scattering plane ($\hat{\mathbf{e}}_\parallel^s = \hat{\mathbf{e}}_\theta$ and $\hat{\mathbf{e}}_\perp^s = -\hat{\mathbf{e}}_\varphi$) let us substitute the Mie coefficients [Eqs. (1.32)] into Eq. (1.27a) while rewriting the VSH $\mathbf{M}_{o1\ell}^{(3)}$ [Eq. (??)] and $\mathbf{N}_{e1\ell}^{(3)}$ [Eq. (??)] in terms of the

Riccati-Bessel function ξ and its derivative:

$$\mathbf{E}^{\mathrm{sca}} \cdot \hat{\mathbf{e}}_r = \frac{\cos\varphi}{(kr)^2} \sum_{\ell}^{\infty} E_0 i^{\ell}(2\ell+1) i a_{\ell} \xi(kr) \pi_{\ell}(\cos\theta)\sin\theta, \tag{1.34a}$$

$$\mathbf{E}^{\mathrm{sca}} \cdot \hat{\mathbf{e}}_{\parallel}^{\mathrm{sca}} = \frac{\cos\varphi}{kr} \sum_{\ell}^{\infty} E_0 i^{\ell} \frac{2\ell+1}{\ell(\ell+1)} [i a_{\ell} \xi_{\ell}'(kr)\tau_{\ell}(\cos\theta) - b_{\ell}\xi_{\ell}(kr)\pi_{\ell}(\cos\theta)], \tag{1.34b}$$

$$\mathbf{E}^{\mathrm{sca}} \cdot \hat{\mathbf{e}}_{\perp}^{\mathrm{sca}} = \frac{\sin\varphi}{-kr} \sum_{\ell}^{\infty} E_0 i^{\ell} \frac{2\ell+1}{\ell(\ell+1)} [i a_{\ell} \xi_{\ell}'(kr)\pi_{\ell}(\cos\theta) - b_{\ell}\xi_{\ell}(kr)\tau_{\ell}(\cos\theta)]. \tag{1.34c}$$

Following a similar procedure but substituting Eq. (1.33) into Eq. (1.27), the internal electric field $\mathbf{E}^{\mathrm{int}}$ can be rewritten also in terms of the Riccati-Bessel functions as

$$\mathbf{E}^{\mathrm{int}} \cdot \hat{\mathbf{e}}_r = -\frac{\cos\varphi}{(k_{\mathrm{p}}r)^2} \sum_{\ell}^{\infty} E_0 i^{\ell}(2\ell+1) i d_{\ell} \psi(k_{\mathrm{p}}r) \pi_{\ell}(\cos\theta)\sin\theta, \tag{1.35a}$$

$$\mathbf{E}^{\mathrm{int}} \cdot \hat{\mathbf{e}}_{\parallel}^{\mathrm{sca}} = \frac{\cos\varphi}{k_{\mathrm{p}}r} \sum_{\ell}^{\infty} E_0 i^{\ell} \frac{2\ell+1}{\ell(\ell+1)} [-i d_{\ell} \psi_{\ell}'(k_{\mathrm{p}}r)\tau_{\ell}(\cos\theta) + c_{\ell}\psi_{\ell}(k_{\mathrm{p}}r)\pi_{\ell}(\cos\theta)], \tag{1.35b}$$

$$\mathbf{E}^{\mathrm{int}} \cdot \hat{\mathbf{e}}_{\perp}^{\mathrm{sca}} = \frac{\sin\varphi}{-k_{\mathrm{p}}r} \sum_{\ell}^{\infty} E_0 i^{\ell} \frac{2\ell+1}{\ell(\ell+1)} [-i d_{\ell} \psi_{\ell}'(k_{\mathrm{p}}r)\pi_{\ell}(\cos\theta) + c_{\ell}\psi_{\ell}(k_{\mathrm{p}}r)\tau_{\ell}(\cos\theta)]. \tag{1.35c}$$

The scattering amplitude matrix relates the incident electric field to the scattered electric field in the far field regime, that its when $kr \gg 1$. Considering that the series of Eqs. (1.34a)-(1.34c) converge uniformly, so all contributions after the sufficiently large term ℓ_c of the sum can be neglected for all values of kr, the asymptotic expressions for the ξ Riccati-Bessel function and its derivative can be employed, which are [4]

$$\xi(kr) \approx (-i)^{\ell} \frac{\exp(ikr)}{i}, \quad \text{and} \quad \frac{\mathrm{d}\xi(kr)}{\mathrm{d}(kr)} = (-i)^{\ell}\exp(ikr)\left(\frac{1}{ikr}+1\right), \quad \text{when} \quad \ell_c^2 \ll kr. \tag{1.36}$$

Substituting Eq. (1.36) into Eqs. (1.34a)-(1.34c) and neglecting terms proportional to $(kr)^{-2}$, it yields a zero radial electric field while

$$\mathbf{E}^{\mathrm{sca}} \cdot \hat{\mathbf{e}}_{\parallel}^{\mathrm{sca}} \approx \frac{\exp(ikr)}{r} \left\{ \frac{i}{k} \sum_{\ell}^{\infty} \frac{2\ell+1}{\ell(\ell+1)} [a_{\ell}\tau_{\ell}(\cos\theta) + b_{\ell}\pi_{\ell}(\cos\theta)] \right\} E_0 \cos\varphi, \tag{1.37a}$$

$$\mathbf{E}^{\mathrm{sca}} \cdot \hat{\mathbf{e}}_{\perp}^{\mathrm{sca}} \approx \frac{\exp(ikr)}{r} \left\{ \frac{i}{k} \sum_{\ell}^{\infty} \frac{2\ell+1}{\ell(\ell+1)} [a_{\ell}\pi_{\ell}(\cos\theta) + b_{\ell}\tau_{\ell}(\cos\theta)] \right\} E_0(-\sin\varphi), \tag{1.37b}$$

where it can be identified that $\mathbf{E}^{\mathrm{i}} \cdot \hat{\mathbf{e}}_{\parallel}^{\mathrm{i}} = E_0 \cos\varphi$ and $\mathbf{E}^{\mathrm{i}} \cdot \hat{\mathbf{e}}_{\perp}^{\mathrm{i}} = -E_0 \sin\varphi$ for $\mathbf{E}^{\mathrm{i}}$ a plane wave traveling along the z direction with an arbitrary polarization. Finally, the scattering amplitude matrix for a spherical particle can be obtained by comparing Eqs. (1.37a) and (1.37b) with Eq. (1.1), yielding

Scattering Amplitude Matrix for Spherical Particles

$$\mathbb{F}(\hat{\mathbf{k}}^{\text{sca}}, \hat{\mathbf{k}}^{\text{i}}) = \begin{pmatrix} \dfrac{i}{k} S_2(\theta) & 0 \\ 0 & \dfrac{i}{k} S_1(\theta) \end{pmatrix}, \tag{1.38}$$

with $\hat{\mathbf{k}}^{\text{sca}} = \hat{\mathbf{e}}_r$, $\hat{\mathbf{k}}^{\text{i}} = \hat{\mathbf{e}}_z$, $\cos\theta = \hat{\mathbf{k}}^{\text{sca}} \cdot \hat{\mathbf{k}}^{\text{i}}$ and

$$S_1(\theta) = \sum_{\ell}^{\infty} \frac{2\ell+1}{\ell(\ell+1)} [a_\ell \tau_\ell(\cos\theta) + b_\ell \pi_\ell(\cos\theta)], \tag{1.39}$$

$$S_2(\theta) = \sum_{\ell}^{\infty} \frac{2\ell+1}{\ell(\ell+1)} [a_\ell \pi_\ell(\cos\theta) + b_\ell \tau_\ell(\cos\theta)], \tag{1.40}$$

which depends entirely on the angular functions $\pi_\ell(\cos\theta)$ and $\tau_\ell(\cos\theta)$ modulated by the Mie coefficients a_ℓ and b_ℓ. The scattering amplitude matrix $\mathbb{F}$ shows the symmetry of the system when it is written in a base relative to the scattering plane, as it was stated in Section 1.1. Since the scatterer is a spherical istropic NP, $\mathbb{F}$ is a diagonal matrix in the base $\{\hat{\mathbf{e}}_\parallel^{\text{sca}}, \hat{\mathbf{e}}_\perp^{\text{sca}}\}$, that is, that the scattered electric field $\mathbf{E}^{\text{sca}}$ maintains the same polarization degree relative to the scattering plane than the incident electric field $\mathbf{E}^{\text{i}}$ that illuminates the spherical particle.

1.2.3 Optical Properties of a Single Spherical (Gold) Particle

In previous Sections, the general theory for the light scattering was developed, introducing the scattering amplitude matrix $\mathbb{F}$ [Eq. (1.1)]. Then, the particular problem of a spherical scatterer was addressed and the explicit expression of the scattered electric field and of $\mathbb{F}$ were obtained [Eq. (1.38)] in terms of the Mie coefficients a_ℓ and b_ℓ [Eqs. (1.32)], as well as the internal electric field inside the scatterer [Eq. (1.37)] in terms of the coefficients c_ℓ and d_ℓ [Eqs. (1.33)]. The optical properties of a particle is related to the electric field outside the scatterer, and can be studied within two different spatial regions: the near field and the far field regimes. The near field regime consists in the complete analytical solution of the scattered electric field [Eq. (1.27a)], while the far field regime considers only its contributions proportional to r^{-1}, with r the distance between the center of the scatterer and the measurement poin; the optical propertiesin the fat field regime can be determined by the scattering amplitude matrix $\mathbb{F}$ alone. In this last Section, the previous results are employed to calculate the optical properties fo a spherical gold nanoparticle (AuNP) with a radius of 12.5 nm, embedded into a matrix of air and into a matrix of glass, when it is illuminated by an incident plane wave with a wavelength λ.

1.2.3.1 Localized Surface Plasmons

The optical properties of a particle, either in the near or the far field regime, are determined by the Mie coefficients a_ℓ and b_ℓ [Eqs. (1.32)] since the exact solution to the scattered electric field $\mathbf{E}^{\text{sca}}$ [[Eq. (1.27a)] is a linear combination of the vector spherical harmonics $\mathbf{N}_{\text{e}1\ell}^{(3)}$ and $\mathbf{M}_{\text{o}1\ell}^{(3)}$ modulated by a_ℓ and b_ℓ, respectively. Thus, the physical interpretation of each term ℓ in the

linear combination, as well as of $\mathbf{N}_{e1\ell}^{(3)}$ and $\mathbf{M}_{o1\ell}^{(3)}$, can be determined by visualizing each one of them independently. By understanding the contribution of each term, the optical response of a particle illuminated by a plane wave can be studied in the near and far regime.

The Figure 1.2 shows the decomposition of the scatttered electric field $\mathbf{E}^{\text{sca}}$ of a spherical particle into its contributions proportional to a_1 [Fig. 1.2a)], b_1 [Fig. 1.2b)], a_2 [Fig. 1.2c)] and b_2 [Fig. 1.2d)], when the particle is illuminated by a x-polarized plane wave traveling in the z direction. The vectorial behavior of the a_ℓ contributions to $\mathbf{E}^{\text{sca}}$ are given by the VSH $\mathbf{N}_{e\ell 1}^{(3)}$ and by $\mathbf{M}_{o\ell 1}^{(3)}$ for the b_ℓ contributions. The scattered electric field is evaluated at a spherical surface (gray sphere) larger than the scatter: the arrow stream on the spherical surface corresponds to the pointing direction of each contribution to $\mathbf{E}^{\text{sca}}$ parallel to the evaluation sphere, while the color code corresponds to the magnitude of the scattered electric field at each point; the solid shape at the center of each axis is a contour surface $\|\mathbf{E}^{\text{sca}}\|$.
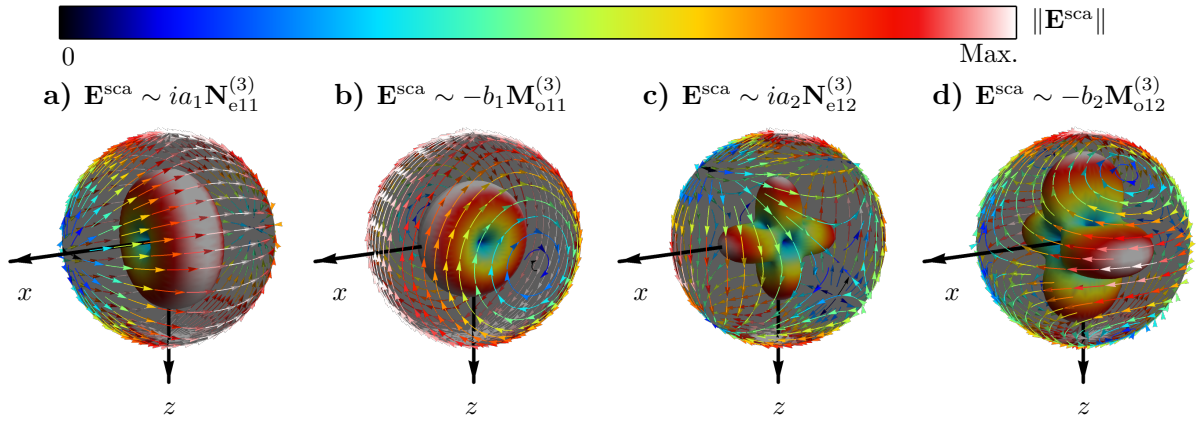
Fig. 1.2: Decomposition of the scattered electric field $\mathbf{E}^{\text{sca}}$ into its contributions proportional to **a)** a_1, **b)** b_1, **c)** a_2 and **d)** b_2 [see Eq. (1.27a)] when a spherical particle (not shown) is illuminated by an x-polarized plane wave traveling in the z direction. The scattered electric field $\mathbf{E}^{\text{sca}}$ is evaluated at a sphere larger than the particle: the arrow stream corresponds to the projection parallel to the evaluation sphere of $\mathbf{E}^{\text{sca}}$ and the color code corresponds to the magnitude of $\mathbf{E}^{\text{sca}}$. A contour surface of the magnitude of $\mathbf{E}^{\text{sca}}$ is located at the center of each axis.

The general effect of each contribution to the scattered electric field $\mathbf{E}^{\text{sca}}$ can be understood by analyzing their behavior around the points where the scattered electric field drops to zero; such points are called nodes and are shown in dark bluish colors in Fig. 1.2. The number of nodes over the evaluation sphere (gray surface) is proportional to the chosen value of ℓ. For example, if $\ell = 1$ [Figs. 1.2a) and 1.2b)] there is a pair of such nodes and if $\ell = 2$ [Figs. 1.2c) and 1.2d)] there are two pairs, where each pair consists of two nodes at opposite sides of the evaluation sphere. When comparing the contributions proportional to a_1 and a_2 [Figs. 1.2a) and 1.2c)] with contributions proportional to b_1 and b_2 [Figs. 1.2b) and 1.2d)], one difference is the location of the pairs of nodes for a fixed value of ℓ, which differ spatially by a rotation around the z axis of an angle $\varphi = \pi/2$. Another difference between the contribution of a_ℓ and the b_ℓ to $\mathbf{E}^{\text{sca}}$ are the trajectories they performed around each pair of nodes: In the a_ℓ contributions the scattered electric field flows from one node to its pair, thus following an open path, while the scattered electric field for the b_ℓ contributions circulates around the nodes forming a closed path. Taking into account such behaviors of the scattered electric field, it can be seen that the a_ℓ (b_ℓ) contribution describes the electric field of an electric (magnetic) dipole when $\ell = 1$ and of an

electric (magnetic) quadrupole when $\ell = 2$. Extrapolating such behavior for an arbitrary ℓ, it can be concluded that the a_ℓ contributions to the scattered electric field, described by the VSH $\mathbf{N}_{\mathrm{e}\ell 1}^{(3)}$, correspond to the electric field of an electric multipole of order ℓ, while the b_ℓ contribution, described by the VSH $\mathbf{M}_{\mathrm{o}\ell 1}^{(3)}$, correspond to the electric field of a magnetic multipole of order ℓ.

The scattered electric field $\mathbf{E}^{\mathrm{sca}}$ of a spherical particle can be written, according to Eq. (1.27a), as a linear contribution of electric fields associated to electric and magnetic multipoles, as shown in Fig. 1.2, modulated by the Mie coefficients a_ℓ and b_ℓ, respectively. Thus, the field $\mathbf{E}^{\mathrm{sca}}$ can reproduce the pattern of a pure electric or magnetic multipole of order ℓ if a_ℓ or b_ℓ are maximized, accordingly. In such cases, the scattered electric field is a standing wave on the surface of the spherical particle known as a Localized Surface Plasmon (LSP). Since the Mie coefficients [Eqs. (1.32)] depend on the material and size of the spherical scatter, on the wavelength and traveling media of the incident plane wave, and on the order ℓ, they values of a_ℓ and b_ℓ are maximized when there is a coupling between the scatterer and the plane wave for a fixed ℓ, which yields a Localized Surface Plasmon Resonance (LSPR). The condition to obtain a LSPR is given by the limit when the denominators of the Eqs. (1.32) tend to zero, that is

$$\xi_\ell(x)\psi_\ell'(mx) - m\psi_\ell(mx)\xi_\ell'(x) \to 0, \qquad \text{(Electric LSPR)}, \qquad (1.41)$$

$$m\xi_\ell(x)\psi_\ell'(mx) - \psi_\ell(mx)\xi_\ell'(x) \to 0, \qquad \text{(Magnetic LSPR)}, \qquad (1.42)$$

where $\psi_\ell(\rho) = \rho j_\ell(\rho)$ and $\xi(\rho) = \rho h_\ell^{(1)}(\rho)$ are the Riccati-Bessel functions, the operator ($'$) denotes the derivative respect to their argument, $x = 2\pi n_{\mathrm{m}}(a/\lambda)$ is the size parameter, with a the radius of the particle and λ the wavelength of the incident plane wave, and $m = n_{\mathrm{p}}/n_{\mathrm{mat}}$ is the contrast between the refractive indices of the particle (n_{p}) and the matrix (n_{m}), both of which are in general wavelength dependent. A more closed condition for the LSPR can be achieved by proposing a model for the refractive index of the particle as it is done in [14] where the Drude Model —see Eq. (B.1) in Appendix B— is employed nevertheless, the roots in Eqs. (1.41) and (1.42) can be found numerically.

The system of interest in this work consists of a spherical gold nanoparticle (AuNP) of radius $a = 12.5$ nm, whose experimental dielectric function is reported by Johnson and Christy [15]. This experimental data corresponds to a bulk sample, meaning that it may not reproduce the optical behavior of a NP since surface effects cannot to be neglected due to their spatial dimensions [16]. In order to study the optical properties of AuNP, for example to determine the conditions for its LSPRs from Eqs. (1.41) and (1.42), while considering surface effects, a size correction to the dielectric function of the AuNP was performed as described in Appendix B. A more detailed discussion on such size effects is performed by analyzing the far field regime in the next section.

The induced electric field $\mathbf{E}^{\mathrm{ind}}$, that is the scattered and internal electric fields, of a spherical AuNP of radius $a = 12.5$ nm were calculated at the conditions of the dipolar ($\ell = 1$) LSPR when the AuNP is embedded into an air matrix ($n_{\mathrm{mat}} = 1$) and when it is illuminated by an x-polarized electric field $\mathbf{E}^{\mathrm{i}}$ traveling in the z direction. In Fig. 1.3 the norm of $\mathbf{E}^{\mathrm{ind}}$ is evaluated at the plane $y = 0$ [Fig. 1.3a)] where the incident electric field is parallel ($\parallel$) to the scattering plane, and at the plane $x = 0$ [Fig. 1.3b)] where the incident electric field is perpendicular ($\perp$) to the scattering plane; in both figures the dashed lines corresponds to the surface of the AuNP. The excitation wavelength λ of the LSPR for the described system was
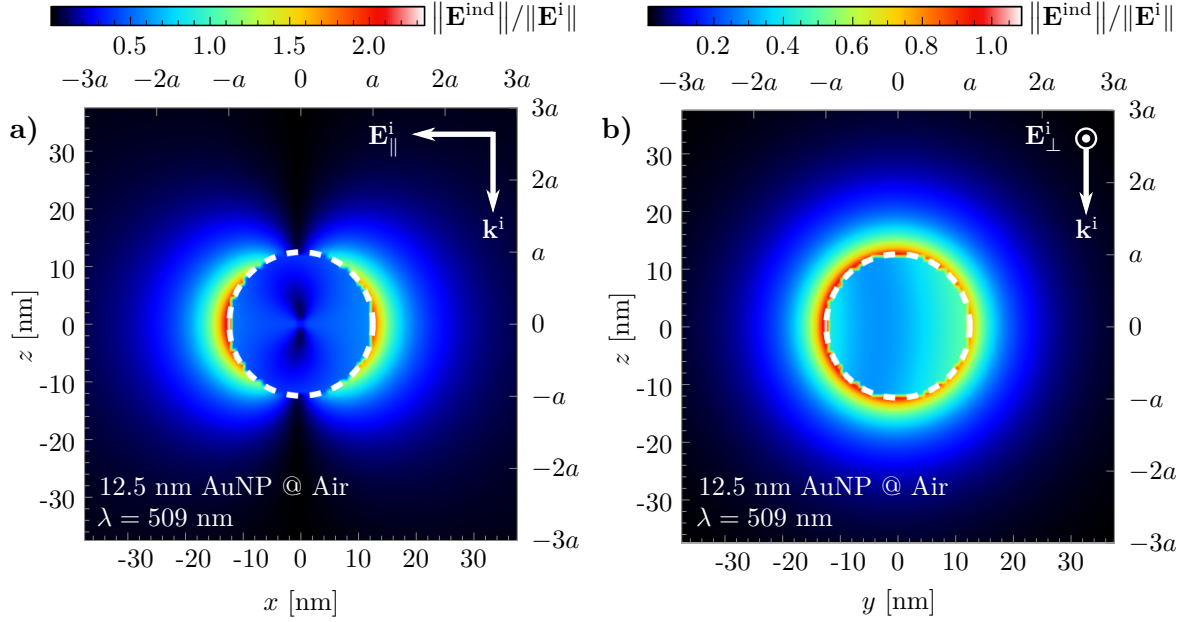
Fig. 1.3: Induced electric field $\mathbf{E}^{\text{int}}$ evaluated at the planes **a)** $y = 0$ and **b)** $x = 0$ of a 12.5 nm Au spherical NP (dashed lines) embedded into air ($n_{\text{mat}} = 1$) when illuminated by an incident plane wave with an x polarized electric field $\mathbf{E}^{\text{i}}$ traveling in the direction $\mathbf{k}^{\text{i}}$ along the z axis with an excitation wavelength $\lambda = 509$ nm of the LSPR. At the plane $x = 0$, the incident electric field is parallel to the scattering plane, while it is perpendicular to it at $x = 0$. The optical response of the 12.5 nm AuNP was modeled by a size correction to the experimental data reported by Johnson and Christy [15].

calculated by employing the size corrected dielectric function for the AuNP in Eq. (1.41).

By comparing the magnitude of the induced electric $\mathbf{E}^{\text{ind}}$ field in Fig. 1.3 outside the AuNP, which was calculated up to the multipolar contribution of $\ell = 7$ accordingly with the Wacombe criteria for convergence [4], with the electric dipolar contribution of the scattered electric field in Fig. 1.2a), the same contour pattern is found. The norm of $\mathbf{E}^{\text{ind}}$ evaluated at a plane parallel to the scattering plane ($y = 0$) shows a contour pattern of two lobes, which is characteristic of an electric dipole. When the induced electric field is evaluated at a perpendicular plane relative to the scattering plane ($x = 0$), the pattern observed corresponds to the azimuthal symmetry of the dipolar electric field. Lastly, it can be seen that there is an enhancement of ~ 2 times of the induced electric field relative to the incident electric field at the surface of the AuNP in the direction parallel to the incident electric field [redish zones in Fig. 1.3a)]; such enhancement corresponds to the LSP.

From the analysis of the electric field scattered by the particle in the near field regime, the LSP can be visualized on the surface of the particle at the conditions imposed by Eq. (1.41) and (1.42) for the electric and magnetic multipoles, respectively. The conditions to excite the LSPR are dictated by the Mie coefficients, therefore the LSPR can also be identified in the far field regime since the amplitude scattering matrix, from which any optical properties in the far field regime can be calculated, is written according to Eq. (1.38) in terms of a_ℓ and b_ℓ. In the following section, the optical properties in the far field regime are calculated and their relation to the LSPR is established, yielding to the observation of the LSPR in the far field.

1.2.3.2 Far Field Optical Properties

The Localized Surface Plasmon Resonance (LSPR) occurs when the scattered electric field of a particle illuminated by a plane wave is described by a stationary wave on the surface of a particle, meaning that it can observed in the near field regime. For a spherical particle, the LSPR occurs when the conditions in Eqs. (1.41) and (1.42) are met, which maximize the Mie coefficients a_ℓ and b_ℓ [Eq. (1.32)], respectively. There are optical properties in the far field regime, that is where only the radiative contributions to the electromagnetic fields are non neglectable, that depend on a_ℓ and b_ℓ, for example, the scattering amplitude matrix $\mathbb{F}$ [Eq. (1.38)]. Therefore, the LSPR can also be identified by analyzing experimental or theoretical results of optical properties such as the scattering C_{sca} and extinction cross sections C_{ext}, which are related to $\mathbb{F}$. Hereby, explicit expressions for the optical properties in the far field regime, for a scattering sphere, are obtained.

By substituting the scattering amplitude matrix for a spherical particle [Eq. (1.38)] into Eqs. (1.8) and (1.12) the scattering C_{sca} and extinction C_{ext} cross sections are obtained; the absorption cross section C_{abs} can be calculated by calculating $C_{\mathrm{ext}} - C_{\mathrm{sca}}$. Assuming an incident plane wave with an x-polarized electric field $\mathbf{E}^{\mathrm{i}}$, and evaluating the scattering amplitude matrix in the forward direction $\theta = 0$, equivalent to $\cos\theta = 1$, the extinction cross section C_{ext} is given by

$$C_{\mathrm{ext}} = \frac{4\pi}{k\|\mathbf{E}^{\mathrm{i}}\|^2} \operatorname{Im}[\frac{i}{k} S_2(\theta = 0)\mathbf{E}^{\mathrm{i}} \cdot \mathbf{E}^{\mathrm{i}*}] = \frac{2\pi}{k^2} \sum_{\ell=1}^{\infty} (2\ell+1)\operatorname{Re}(a_\ell + b_\ell), \qquad (1.43)$$

where the Eq. (A.16) in Appendix A was employed to tevaluate the angular functions $\pi_\ell(\cos\theta)$ and $\tau_\ell(\cos\theta)$. In a similar manner, the scattering cross section C_{sca} can be written as

$$C_{\mathrm{sca}} = \int_0^{2\pi} \int_0^{\pi} \frac{(iS_2(\theta)\mathbf{E}^{\mathrm{i}})^*(iS_2(\theta)\mathbf{E}^{\mathrm{i}})}{k^2\mathbf{E}^{\mathrm{i}}} \sin\theta \, \mathrm{d}\varphi \, \mathrm{d}\theta = \frac{2\pi}{k^2} \sum_{\ell=1}^{\infty} (2\ell+1)(|a_\ell|^2 + |b_\ell|^2), \qquad (1.44)$$

where the orthogonality relations of $\pi_\ell(\cos\theta) \pm \tau_\ell(\cos\theta)$ [Eq. (A.20) in Appendix A] were used. In order to compare the absorption, scattering or extinction of light by a spherical particle, independently of its radius a or embedding media (matrix), it is convenient to define the efficiencies of absorption Q_{abs}, scattering Q_{sca} and extinction Q_{ext} by normalizing the absorption, scattering and extinction cross sections by the geometrical cross section of the spherical particle, yielding the dimensionless expressions

$$\frac{C_{\mathrm{ext}}}{\pi a^2} = \frac{C_{\mathrm{abs}}}{\pi a^2} + \frac{C_{\mathrm{sca}}}{\pi a^2} \qquad \longrightarrow \qquad Q_{\mathrm{ext}} = Q_{\mathrm{abs}} + Q_{\mathrm{sca}}. \qquad (1.45)$$

The Eq. (1.45), along with optical theorem [Eq. (1.11)], states that the extinction of light considers the combination of both absorption and scattering mechanisms. Since the analytical expression of C_{ext} for a spherical particle [Eq. (1.43) is proportional to the real parts of the Mie coefficients a_ℓ and b_ℓ, then it is also maximized at the LSPR. Therefore, the LSPR can be observed in the far field by calculating or measuring the extinction cross section.

In order to study the LSPR of a spherical AuNP of radius $a = 12.5$ nm, the extinction Q_{ext} and the scattering Q_{sca} efficiencies are shown in Fig. 1.4, as function of the wavelength λ of

the incident plane wave illuminating the NP. Two different matrices were considered: a matrix of air with a refractive index of $n_{mat} = 1$ (black lines) and of glass with $n_{mat} = 1.5$ (orange lines). The optical response of the AuNP was modeled by a dielectric function considering the raw data (solid lines) from Johnson and Christy [15], and a size correction to it (dashed lines). In all cases, the LSPR wavelength is indicated in the figure at the maximum of the extinction efficiencies and the wavlength of maximum scattering is also indicated.
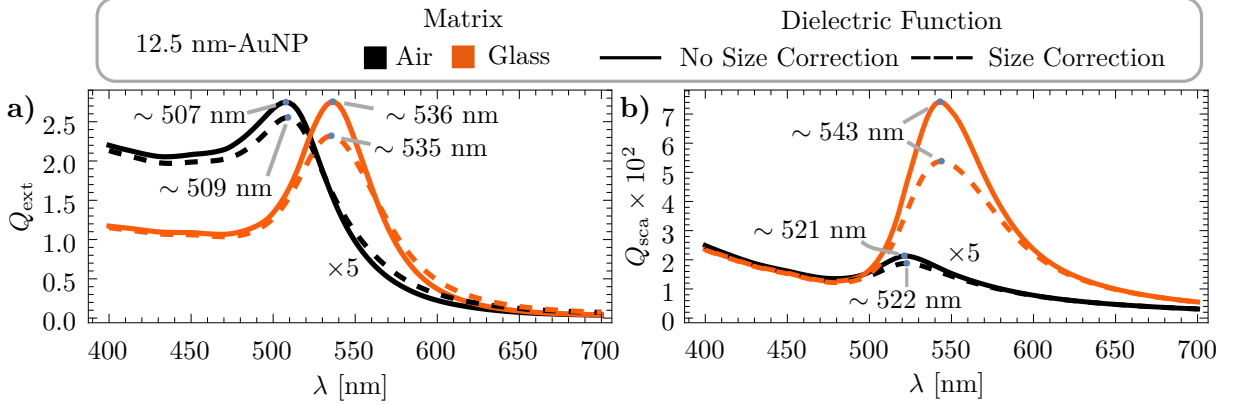
Fig. 1.4: a) Extinction Q_{ext} and **b)** scattering Q_{sca} efficiencies of a 12.5 nm Au spherical NP embeded into air (black, $n_{mat} = 1$) and into galss (orange, $n_{mat} = 1.33$), as function of the wavelength λ of the incident plane wave. The solid curves were calculated by considering no size effects on the dielectric function of the AuNP, while the dashed curves consider a size correction to it; the experimental data of Johnson and Christy [15] was employed.

By comparing Figs. 1.4a) and 2.7b), it is determined that the main loss mechanism in the system is absorption since Q_{sca} is two orders of magnitude smaller than Q_{ext} for all λ in the visible spectrum. Yet, another difference between Q_{sca} and Q_{ext} is the value of λ that maximizes them: for the chosen system the λ of maximum scattering is redshifted ~ 12 nm from LSPR excitation wavelength in all cases. On the other size, an effect common for both the scattering and the extinction efficiencies is an overall enhancement when the refractive index of the matrix increases, as well as a redshift of ~ 25 nm of the LSPR excitation wavelength and the wavelength of maximum scattering —compare the black curves ($n_{mat} = 1$, air) with the orange ones ($n_{mat} = 1.5$, glass)—, which can be understood by analyzing the size parameter $x = (2\pi/\lambda)an_{mat}$. Since x is a linear function of n_{mat}, the AuNP embedded into glass optically responds like a larger NP than what it is in air, thus having a more significant contribution from the scattering to the light extinction mechanism inside glass, as well as an increase in the absorption.

The effect of the size correction to the dielectric function of the AuNP can be understood by comparing the solid and dashed lines. On the one hand, there is a spectral shift of the LSPR excitation wavelength of ~ 2 nm. On the other hand, the value of the efficiencies around the wavelength where the extinction and the scattering is maximized decreases in all cases shown if Fig. 1.4. This behavior can be explained by how the size correction is performed: as explained in Appendix B, the surface effects are taken into account by introducing a smaller mean free path for the free electrons inside the AuNP, therefore increasing the value of the damping constant and thus leading to a larger imaginary part for the dielectric functions employed, which is related to the absorption mechanisms [17]. The decrease in the efficiencies due to a size corrected dielectric function is more evident for a matrix of glass than of air, since the AuNP is optically bigger in such matrix as explained above. From this analysis it can be concluded that the most notable
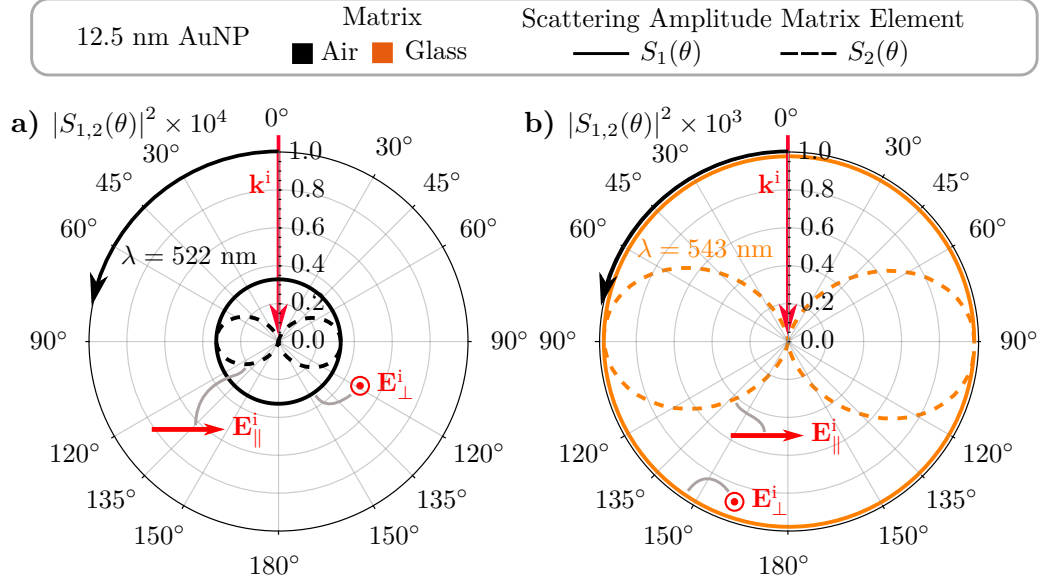
Fig. 1.5: Radiation pattern of a 12.5 nm Au spherical NP embeded into **a)** air illuminatated by a plane wave at a wavelength of $\lambda = 522$ nm and **b)** glass illuminated at $\lambda = 543$ nm; the wavlength in each case corresponds to the wavelength of maximum scattering (see Fig. 1.4). The solid (dashed) lines corresponds to the scattering matrix element S_1 (S_2) related to an incident electric field $\mathbf{E}^i$ travelling in the $\mathbf{k}^i$ direction and polarized perpendicularly (prallel) to the page. It was considered for both matrices a size corretion to the experimental data of Johnson and Christy [15] for the electromagnetic response of the AuNP.

effect of a size correction to the dielectric function of a NP is the decrease in the extinction and scattering efficiencies, while there is still a spectral shift of the LSPR, whose effect is less relevant the larger the size parameter is.

While the scattering efficiency Q_{sca} is an integral quantity, that is, it describes the scattering in all directions of a plane wave traveling in the direction $\mathbf{k}^i$ due to the interaction with a NP, the scattering amplitude matrix elements $S_1(\theta)$, given for a spherical NP by Eq. (1.39), and $S_2(\theta)$, by Eq. (1.40), depict the electric field $\mathbf{E}^s$, at a measurement angle θ, scattered by a NP polarized in a direction perpendicular ($\perp$) to the scattering plane and parallel ($\parallel$) to it, respectively. A radiation pattern helps to vizualize the behavior of $S_{1,2}(\theta)$, a dimensionless parameter such as the scattering efficiency, by plotting their squared modulus as function of θ, as it is shown in for a 12.5 nm AuNP in Fig. 1.5, where $|S_1(\theta)|^2$ (solid lines) and $|S_2(\theta)|^2$ (dashed lines) are shown for two different scenarios: a AuNP embedded into air [Fig. 1.5a), black curves] illuminated at a wavelength $\lambda = 522$ nm and a AuNP embedded into glass [Fig. 1.5b), orange curves] illuminated at $\lambda = 543$ nm. The wavelengths of the incident plane wave corresponds to the value of λ where Q_{sca} is maximized for each matrix as seen in Fig. 1.4.

The quantities $|S_{1,2}(\theta)|^2$ for a 12.5 nm AuNP embedded into air ($n_{\mathrm{mat}} = 1$, black curves) are one order of magnitude smaller than into glass ($n_{\mathrm{mat}} = 1.5$, orange curves), meaning that the AuNP scatters light less efficiently in air than in glass, which is consistent with the obtained values for the scattering efficiency Q_{sca} in Fig. 1.4. On the angular dependency, the radiation pattern of the AuNP in both matrices follow the same tendencies: an homogeneous scattered electric field when the AuNP scatters the perpendicularly polarized incident electric field $\mathbf{E}^s_\perp$ (continuous lines), and a two-lobes pattern when illuminated with a parallel polarized $\mathbf{E}^i$. The observed radiation pattern can be identify in the near field regime, see Fig. 1.3, nevertheless

within the radiation pattern analysis, the presence of the LSPR is lost, unlike within an analysis of the extinction cross section.

The Finite Element Method

Several physical problems are described by systems of partial differential equations (PDE) alongside boundary or initial conditions, whose analytical solution can be achieved only in some cases. For example, the scattering of light due to an arbitrary spherical particle, described by the vectorial Helmholtz equation [Eq. (1.13)] with the boundary conditions at the surface of the spherical particle given by Eq. (1.26), is one of the few physical problem with an analytical solution nevertheless, it is set in an ideal scenario where the particle is a perfect sphere, it is isolated and embebed into a non-absorbing matrix and, even more, an harmonic time-dependent incident electric plane wave was assumed. Any of these conditions on the geometry and physical properties of the described system were to change, the scattering problem may not have an analytical solution or it may be to hard to compute even though the solution have already been found[1]; for such cases one alternative is to employ a numerical approach to find an approximated solution to the physical problem. Among the numerical methods commonly employed in electrodynamics one can find the Finite-difference time-domain method, the Boundary Element Method and the Finite Element Method (FEM); the later is a general method for any set of PDE system while the others are specifically numerical solutions to Maxwell's Equations.

In this work the problem of the light scattering due to a spherical particle, whose analytical solution is give by the Mie Theory, was modified by introducing a second medium, a substrate, forming a planar interface with the matrix and allowing the spherical particle to be partially embedded into both the matrix and the substrate. To solve this problem

---

[1] **Poner la solucion analitica de un esferoide pero retomando que es poco estable.**

2.1 Fundamentals

2.1.1 Weak Formulation and the Galerkin Method

2.1.2 Elements

2.2 Formulation of the Light Scattering on the Finite Element Method

2.3 Finite Element Method and Analytical Solutions
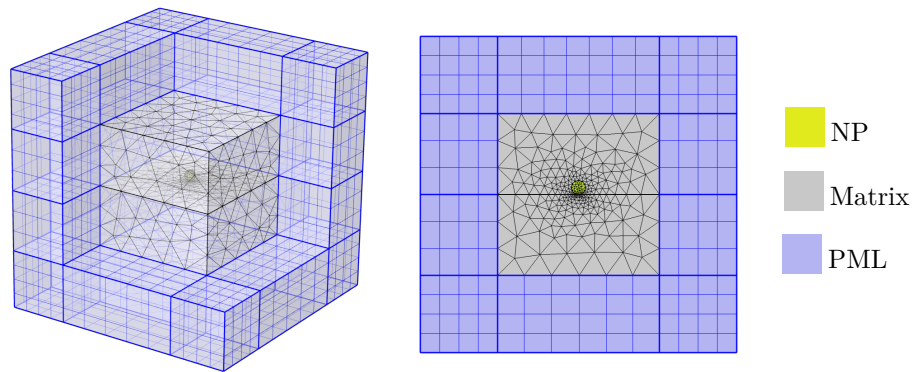
Fig. 2.1: A 3D view (left) and the cross section (right) of a spherical symmetric COMSOL setup to calculate the optical response of a single spherical NP embedded into a matrix. The NP (yellow) is located at the center of the matrix (gray), which is covered by a PML layer (blue). The upper layer of the PML is hidden to allow a better view of the setup.
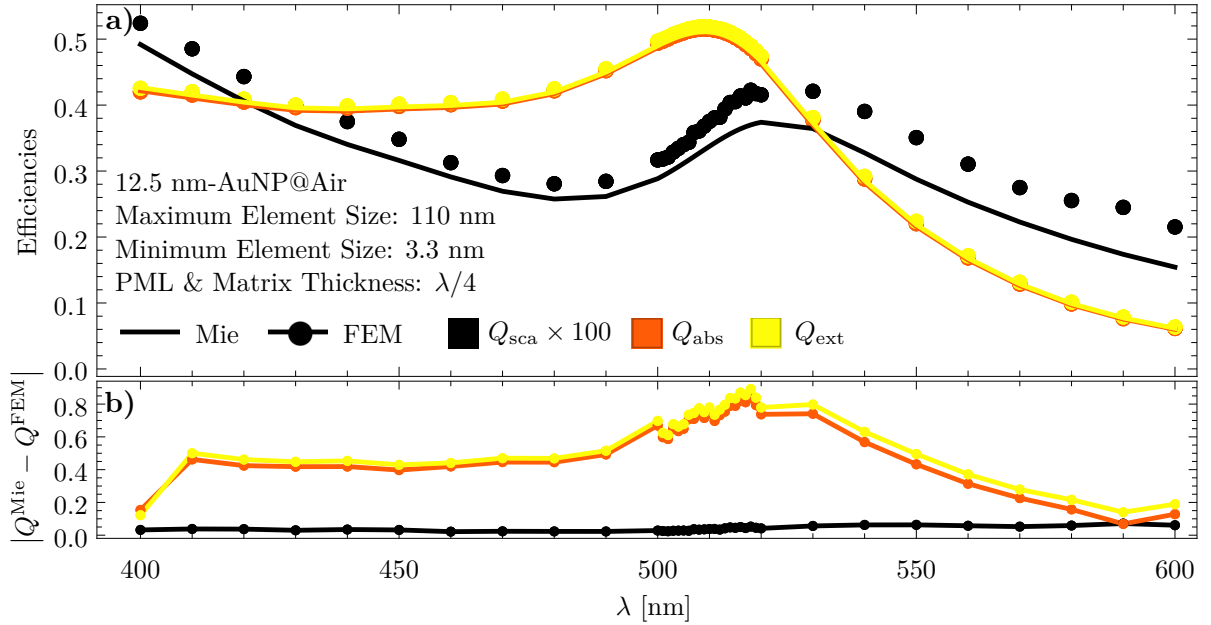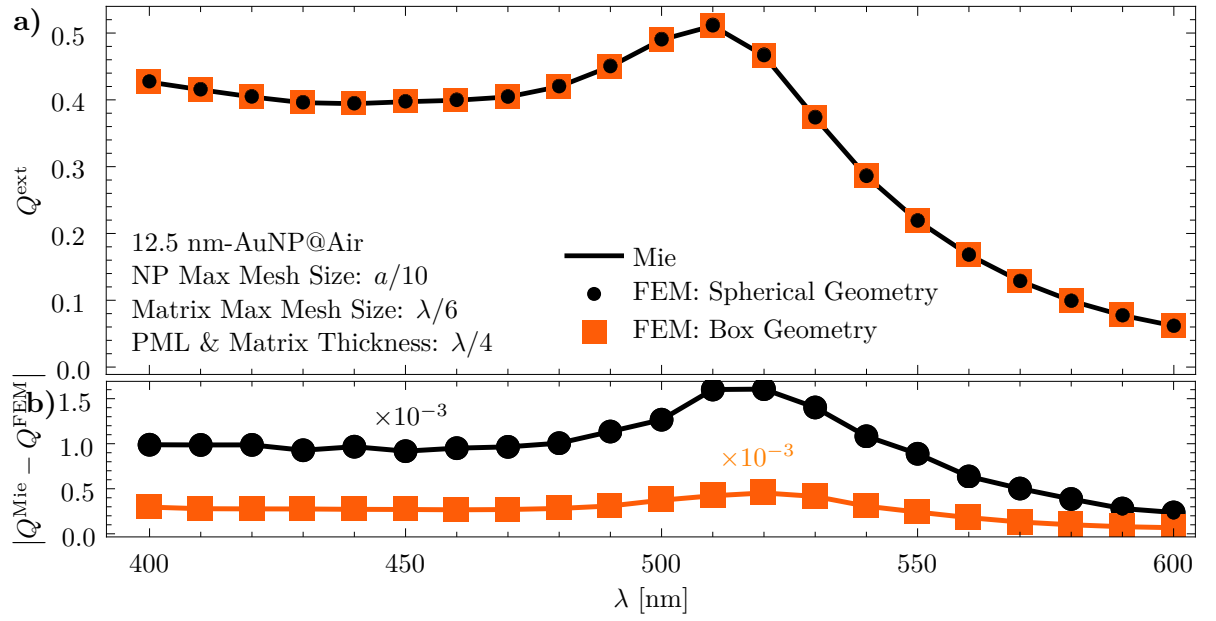
Fig. 2.2: **a)** Scattering Q_{sca}, absorption Q_{abs} and extinction Q_{ext} efficiencies of a 5 nm AuNP embedded into air calculated by means of the Mie Theory (continuous) and the FEM (disks), and **b)** their absolute error, as function of the wavelength λ of the incident plane wave. The chosen parameters for the FEM calculations were based on the COMSOL Excercises **CITAR**.
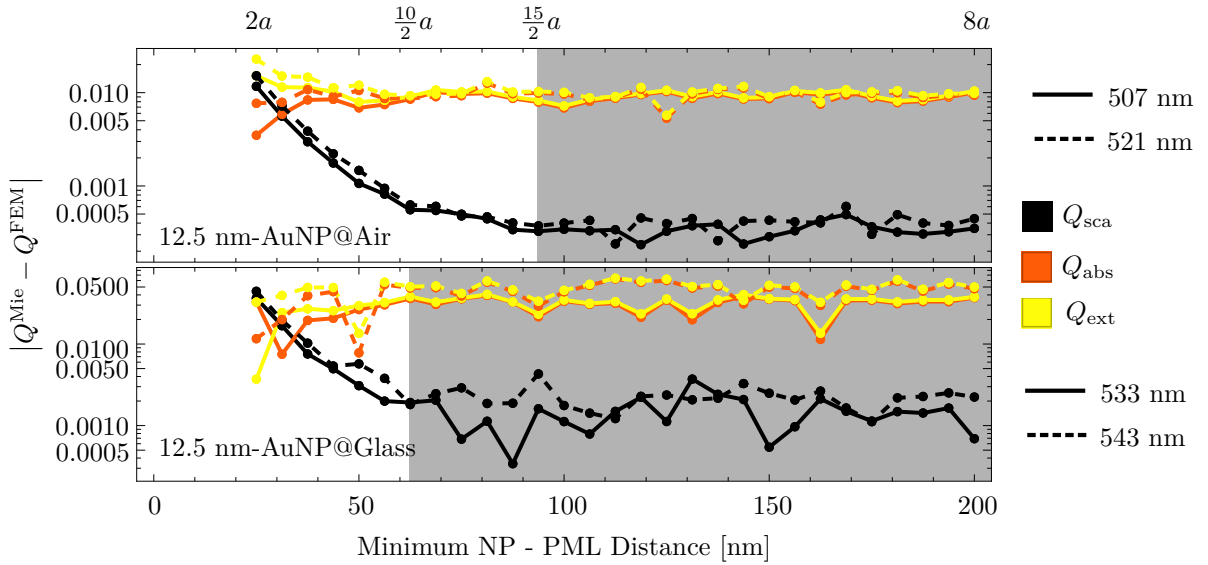
Fig. 2.3: Absolute error between the Mie Theory and the FEM calculation on the extinction efficiency Q_{ext} of a 5nm AuNP@Air as function of the maximum mesh size within the NP at the wavelength of the LSPR.
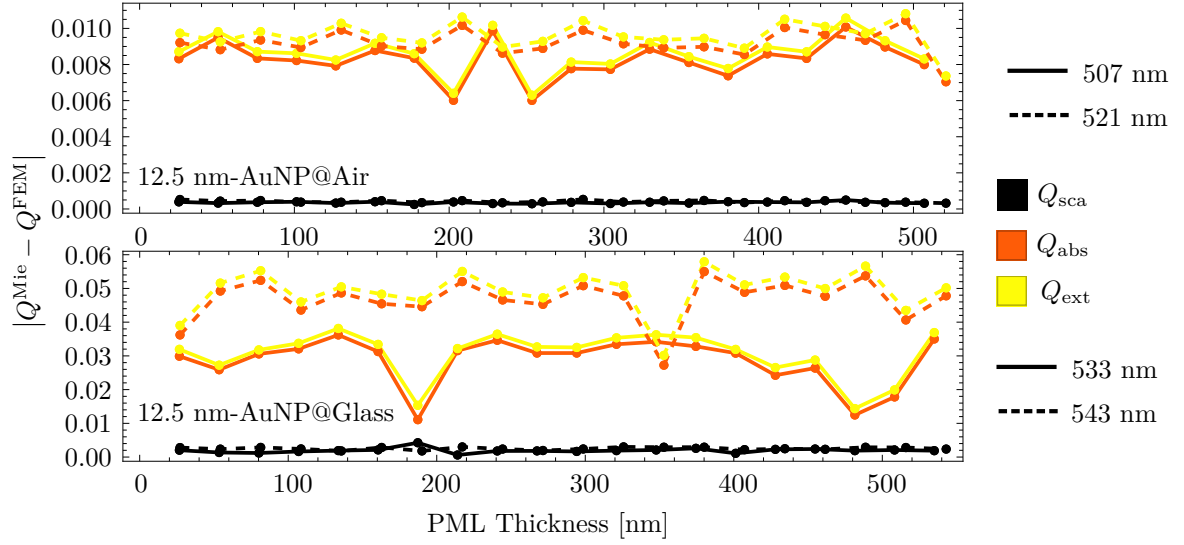
Fig. 2.4: Absolute error between the Mie Theory and the FEM calculation on the extinction efficiency Q_{ext} of a 5nm AuNP@Air as function of the maximum mesh size within the matrix at the wavelength of the LSPR.
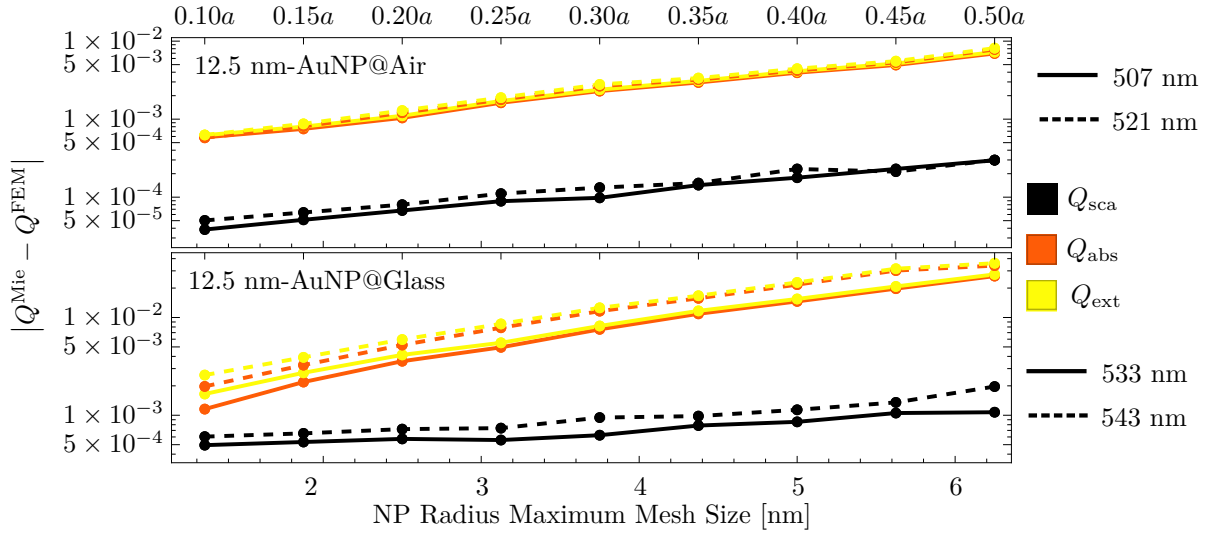
Fig. 2.5: Absolute error between the Mie Theory and the FEM calculation on the extinction efficiency Q_{ext} of a 5nm AuNP@Air as function of the matrix thickness (black) and the PML thickness (orange) at the wavelength of the LSPR. It wac chosen for both cases a NP maximum mesh size of $a/10$ and a matrix maximum mesh size of $\lambda/6$; the default thickness of the matrix and PML was set to $\lambda/4$.

Fig. 2.6: A 3D view (left) and the cross section (right) of a spherical symmetric COMSOL setup to calculate the optical response of a single spherical NP embedded into a matrix. The NP (yellow) is located at the center of the matrix (gray), which is covered by a PML layer (blue). The upper layer of the PML is hidden to allow a better view of the setup.

Fig. 2.7: a) Scattering Q_{sca}, absorption Q_{abs} and extinction Q_{ext} efficiencies of a 5 nm AuNP embedded into air calculated by means of the Mie Theory (continuous) and the FEM (disks), and **b)** their absolute error, as function of the wavelength λ of the incident plane wave. The chosen parameters for the FEM calculations were based on the COMSOL Excercises **CITAR**.

Results and Discussion

3.1 Incrustation Degree of a Spherical Particle

3.2 Future Work: Application on Metasurfaces
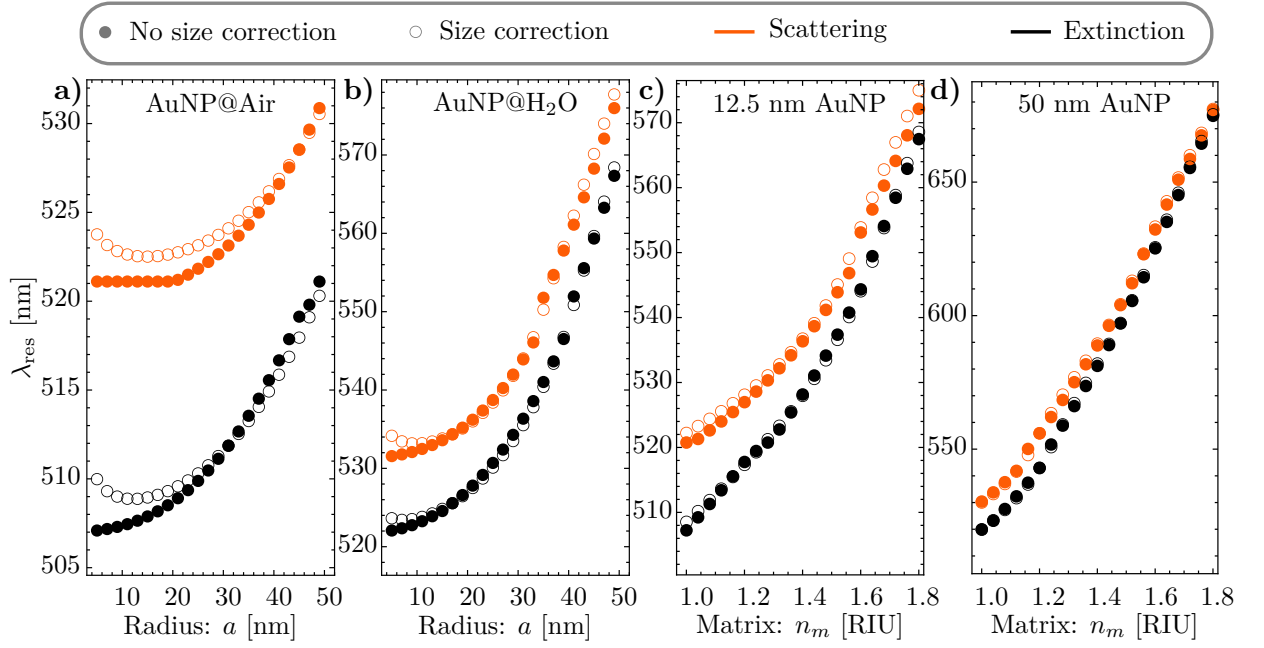
Fig. 3.1: Resonance wavlength (λ_{res}) of the scattering (orange) and extinction (black) cross sections as functions of the NPs radii when embedded 3.1a) into air and 3.1b) into water, and as function of the refractive index of the matrix for NP of radius set to 3.1c) 12.5 nm and 3.1d) 50 nm.

Conclusions

Mie Theory (Conventions and Code)

The Vector Spherical Harmonics (VSH) where defined in Sec. 1.2.1 in terms of their generating function $\psi(r, \theta, \varphi)$ which must satisfy the scalar Helmholtz equation [Eq. (1.15)]. By employing the separation of variables method, it was determined that ψ is the product of either $\sin(m\varphi)$ or $\cos(m\varphi)$, of the associated Legendre functions $P_\ell^m(\cos\theta)$ and the spherical Bessel/Hankel functions $z_\ell(kr)$, all of which are solutions to Eqs. (1.16)-(1.20). In this section, it is discussed the chosen definitions for P_ℓ^m, z_ℓ and related functions, as well as how to calculate them. It is also detailed how to code the Mie Theory results employing the Wolfram Language.

Radial Dependency: Spherical Bessel/Hankel Functions

The radial dependency of the VSH is given by the two linearly independent solutions to Eq. (1.20) which are the spherical Bessel function of first and second kind $j_\ell(\rho)$ and $y_\ell(\rho)$, respectively, related by the regular Bessel function of fractional order $J_{\ell+1/2}(\rho)$ and $Y_{\ell+1/2}(\rho)$ by

$$j_\ell(\rho) = \sqrt{\frac{\pi}{2\rho}} J_{\ell+1/2}(\rho), \quad \text{and} \quad y_\ell(\rho) = \sqrt{\frac{\pi}{2\rho}} Y_{\ell+1/2}(\rho). \tag{A.1}$$

Another set of two linear independent solutions to Eq. (1.20) are the spherical Hankel functions of first $(h_\ell^{(1)})$ and second kind $(h_\ell^{(1)})$ given by

$$h_\ell^{(1)}(\rho) = j_\ell(\rho) + iy_\ell(\rho), \quad \text{and} \quad h_\ell^{(2)}(\rho) = j_\ell(\rho) - iy_\ell(\rho). \tag{A.2}$$

Since the spherical Hankel functions are a linear combination of the Bessel spherical functions, they four obey the following recurrence relations

$$\frac{z_\ell(\rho)}{\rho} = \frac{z_{\ell-1}(\rho) + z_{\ell+1}(\rho)}{2\ell + 1}, \tag{A.3}$$

$$\frac{\mathrm{d}z_\ell(\rho)}{\mathrm{d}\rho} = \frac{\ell z_{\ell-1}(\rho) - (\ell+1)z_{\ell+1}(\rho)}{2\ell + 1}, \tag{A.4}$$

with z_ℓ any of the functions in Eqs. (A.1) and (A.2).

Azimuthal Angular Dependency φ: Sine, Cosine

Within this text, it was chosen the azimuthal solution to the scalar Helmholtz equation to be sines and cosines, so m can only take non negative integer values. This functions obey the orthogonality relations

$$\int_0^{2\pi} \sin(m\varphi)\sin(m'\varphi)\,\mathrm{d}\varphi = \delta_{m,m'}(1 - \delta_{0,m})\pi, \tag{A.5}$$

$$\int_0^{2\pi} \cos(m\varphi)\cos(m'\varphi)\,\mathrm{d}\varphi = \delta_{m,m'}(1 + \delta_{0,m})\pi, \tag{A.6}$$

$$\int_0^{2\pi} \cos(m\varphi)\sin(m'\varphi)\,\mathrm{d}\varphi = 0, \tag{A.7}$$

with $\delta_{m,m'}$ the Kroneker delta.

Polar Angular Dependency: Associated Legendre Functions and the Angular Functions π_ℓ and τ_ℓ

The solution to the polar angle equation are the associated Legendre functions and in this work they are defined as by Arfken and Weber [18], that is,

$$P_\ell^m(\mu) = (1 - \mu^2)^{m/2}\frac{\mathrm{d}^m}{\mathrm{d}\mu^m}P_\ell(\mu), \quad \text{with} \quad P_\ell(\mu) = \frac{1}{2^\ell \ell!}\frac{\mathrm{d}^\ell}{\mathrm{d}\mu^\ell}(\mu^2 - 1)^\ell, \tag{A.8}$$

where $\mu = \cos\theta$ and $P_\ell(\mu)$ are the Legendre polynomials with ℓ a non negative integer. With such definition, the associated Legendre functions follows the orthogonality relation

$$\int_{-1}^1 P_\ell^m(\mu)P_{\ell'}^m(\mu)\,\mathrm{d}\mu = \frac{2\delta_{\ell,\ell'}}{2\ell + 1}\frac{(\ell + m)!}{(\ell - m)!}. \tag{A.9}$$

It was shown in Section 1.2.2 that the a plane wave can be written as a linear combination of the VSH with only $m = 1$, which lead to the definition of the angular functions π_ℓ and τ_ℓ given by

$$\pi_\ell(\cos\theta) = \frac{P_\ell^1(\cos\theta)}{\sin\theta}, \quad \text{and} \quad \tau_\ell(\cos\theta) = \frac{\mathrm{d}P_\ell^1(\cos\theta)}{\mathrm{d}\theta},$$

which can be calculated recursively with Eq. (A.8) and the recurrence relations of the Legendre polynomials

$$(2\ell - 1)\mu P_{\ell-1}(\mu) = (\ell - 1)P_\ell(\mu) + \ell P_{\ell-2}(\mu), \tag{A.10}$$

$$(1 - \mu^2)^2\frac{\mathrm{d}P_\ell(\mu)}{\mathrm{d}\mu} = \ell P_{\ell-1}(\mu) - \ell\mu P_\ell(\mu). \tag{A.11}$$

leading to

$$\pi_\ell(\mu) = \frac{2\ell - 1}{\ell - 1} \mu \pi_{\ell-1}(\mu) - \frac{\ell}{\ell - 1} \tau_{\ell-2}, \tag{A.12}$$

$$\tau_\ell(\mu) = \ell \mu \pi_\ell(\mu) - (\ell + 1)\pi_{\ell-2}(\mu). \tag{A.13}$$

where $\pi_1(\mu) = 1$ according to Eq. (A.8) and where $\pi_0(\mu) = 0$ is defined. Another notable result from Eq. (A.8) is that the angular functions $\pi_\ell(\mu)$ and $\tau_\ell(\mu)$, when evaluated at $\theta = 0$ ($\mu = 1$), follows

$$\pi_\ell(\mu = 1) = \left. \frac{\mathrm{d}P_\ell(\mu)}{\mathrm{d}\mu} \right|_{\mu=1}, \tag{A.14}$$

$$\tau_\ell(\mu = 1) = \left[\frac{\mathrm{d}P_\ell^1(\mu)}{\mathrm{d}\mu} + (1 - \mu^2)^{1/2} \frac{\mathrm{d}^2 P_\ell(\mu)}{\mathrm{d}\mu^2} \right]\Bigg|_{\mu=1} = \left. \frac{\mathrm{d}P_\ell(\mu)}{\mathrm{d}\mu} \right|_{\mu=1}, \tag{A.15}$$

which can be obtained from the Legendre equation by setting $m = 1$ and $\mu = 1$ in Eq. (1.19), leading to

$$\pi_\ell(\mu = 1) = \tau_\ell(\mu = 1) = \frac{\ell(\ell + 1)}{2} P_\ell(\mu = 1) = \frac{\ell(\ell + 1)}{2}, \tag{A.16}$$

where the last equality arises from the chosen definition of the Legendre polynomial [Eq. (A.8)].

The angular functions π_ℓ and τ_ℓ are not orthogonal in general, nevertheless $\pi_\ell(\mu) \pm \tau_\ell(\mu)$ are. To prove the orthogonality of $\pi_\ell \pm \tau_\ell$ let us apply the Legendre equation [Eq. (1.17)] to P_ℓ^m and multiply it by $P_{\ell'}^m$; repeating this procedure inverting ℓ and ℓ' and adding both equations it is obtained that

$$\frac{\mathrm{d}}{\mathrm{d}\theta}\left(\sin\theta P_{\ell'}^m(\mu) \frac{\mathrm{d}P_\ell^m(\mu)}{\mathrm{d}\theta} \right) + \frac{\mathrm{d}}{\mathrm{d}\theta}\left(\sin\theta P_\ell^m(\mu) \frac{\mathrm{d}P_{\ell'}^m(\mu)}{\mathrm{d}\theta} \right) + \tag{A.17}$$

$$[\ell(\ell+1) + \ell'(\ell'+1)] P_{\ell'}^m(\mu) P_\ell^m(\mu) \sin\theta = 2\left(\frac{m P_\ell^m(\mu)}{\sin\theta} \frac{m P_{\ell'}^m(\mu)}{\sin\theta} + \frac{\mathrm{d}P_\ell^m(\mu)}{\mathrm{d}\theta} \frac{\mathrm{d}P_{\ell'}^m(\mu)}{\mathrm{d}\theta} \right) \sin\theta,$$

where it was added $2\, \mathrm{d}P_\ell^m/\mathrm{d}\theta\ \mathrm{d}P_{\ell'}^m/\mathrm{d}\theta$ on both sides to complete the derivatives. Integrating Eq. (A.17) in th interval $\theta \in (0, \pi)$, or $\mu \in (-1, 1)$, and employing Eqs. (A.8) and (A.9), one obtains that

$$\int_{-1}^{1} \left(\frac{m P_\ell^m(\mu)}{\sin\theta} \frac{m P_{\ell'}^m(\mu)}{\sin\theta} + \frac{\mathrm{d}P_\ell^m(\mu)}{\mathrm{d}\theta} \frac{\mathrm{d}P_{\ell'}^m(\mu)}{\mathrm{d}\theta} \right) \mathrm{d}\mu = \delta_{\ell,\ell'} \frac{2\ell(\ell+1)}{2\ell+1} \frac{(\ell+m)!}{(\ell-m)!}. \tag{A.18}$$

Additionally

$$\int_{-1}^{1} \frac{m P_\ell^m(\mu)}{\sin\theta} \frac{\mathrm{d}P_{\ell'}^m(\mu)}{\mathrm{d}\theta} \mathrm{d}\mu = \int_0^\pi m P_\ell^m(\mu) \frac{\mathrm{d}P_{\ell'}^m(\mu)}{\mathrm{d}\theta} \mathrm{d}\theta = -\int_{-1}^{1} \frac{m P_{\ell'}^m(\mu)}{\sin\theta} \frac{\mathrm{d}P_\ell^m(\mu)}{\mathrm{d}\theta} \mathrm{d}\mu. \tag{A.19}$$

where Eq. (A.8) was employed along integration by parts. Thus, combining Eqs. (A.18) and (A.19), it leads to

$$\int_{-1}^{1} \left(\frac{m P_\ell^m(\mu)}{\sin\theta} \pm \frac{\mathrm{d}P_\ell^m(\mu)}{\mathrm{d}\theta} \right) \left(\frac{m P_{\ell'}^m(\mu)}{\sin\theta} \pm \frac{\mathrm{d}P_{\ell'}^m(\mu)}{\mathrm{d}\theta} \right) \mathrm{d}\mu = \delta_{\ell,\ell'} \frac{2\ell(\ell+1)}{2\ell+1} \frac{(\ell+m)!}{(\ell-m)!}. \tag{A.20}$$

The Eq. (A.20) is the orthogonality of $\pi_\ell(\mu) \pm \tau_\ell(\mu)$ when $m = 1$, which also simplifies the right hand side to $\delta_{\ell,\ell'} 2\ell^2 (l + 1)^2/(2\ell + 1)$.

Vector Spherical Harmonics Orthogonality Relations

The VSH follow orthogonality relations inherited from the orthogonality of sine, cosine and the associated Legendre functions. Let us define the inner product as the integral in the solid angle between two vector functions as

$$\langle \mathbf{A}, \mathbf{A}' \rangle_\Omega = \int_0^{2\pi} \int_0^\pi \mathbf{A} \cdot \mathbf{A}' \sin\theta \, \mathrm{d}\theta \, \mathrm{d}\varphi \,. \tag{A.21}$$

Under this inner product, all even VSH are orthogonal to the odd VSH, as well as all VSH with $m \neq m'$, due to the orthogonality of $\sin(m\varphi)$ and $\cos(m'\varphi)$. The remaining orthogonality relations can be obtained by employing Eq. (A.18), leading to

$$\langle \mathbf{L}_{em'\ell}, \mathbf{L}_{em'\ell'} \rangle_\Omega = \langle \mathbf{L}_{om\ell}, \mathbf{L}_{om\ell'} \rangle_\Omega$$
$$= \delta_{m,m'} \delta_{\ell,\ell'} (1 \pm \delta_{m,0}) \frac{2\pi}{2\ell + 1} \frac{(\ell + m)!}{(\ell - m)!} \left[\left(k \frac{\mathrm{d}z_\ell(kr)}{\mathrm{d}(kr)} \right)^2 + \ell(\ell + 1) \left(k \frac{z_\ell(kr)}{kr} \right)^2 \right], \tag{A.22}$$

$$\langle \mathbf{M}_{em\ell}, \mathbf{M}_{em\ell'} \rangle_\Omega = \langle \mathbf{M}_{om\ell}, \mathbf{M}_{om\ell'} \rangle_\Omega$$
$$= \delta_{m,m'} \delta_{\ell,\ell'} (1 \pm \delta_{m,0}) \pi \frac{2\ell(\ell + 1)}{2\ell + 1} \frac{(\ell + m)!}{(\ell - m)!} z_\ell^2(kr), \tag{A.23}$$

$$\langle \mathbf{N}_{em\ell}, \mathbf{N}_{em\ell'} \rangle_\Omega = \langle \mathbf{N}_{om\ell}, \mathbf{N}_{om\ell'} \rangle_\Omega$$
$$= \delta_{m,m'} \delta_{\ell,\ell'} (1 \pm \delta_{m,0}) \pi \frac{2\ell(\ell + 1)}{2\ell + 1} \frac{(\ell + m)!}{(\ell - m)!} \left[\left(\frac{z_\ell}{kr} \right)^2 + \left(\frac{1}{kr} \frac{\mathrm{d}[krz_\ell(kr)]}{\mathrm{d}(kr)} \right)^2 \right]. \tag{A.24}$$

$$\langle \mathbf{L}_{em\ell}, \mathbf{N}_{em\ell'} \rangle_\Omega = \langle \mathbf{L}_{om\ell}, \mathbf{N}_{om\ell'} \rangle_\Omega$$
$$= \delta_{m,m'} \delta_{\ell,\ell'} (1 \pm \delta_{m,0}) \pi \frac{2\ell(\ell + 1)}{2\ell + 1} \frac{(\ell + m)!}{(\ell - m)!} \left[\frac{z_\ell}{kr} \frac{\mathrm{d}z_\ell(kr)}{\mathrm{d}(kr)} + \left(\frac{1}{kr} \frac{\mathrm{d}[krz_\ell(kr)]}{\mathrm{d}(kr)} \right)^2 \right] \tag{A.25}$$

where $(1 + \delta_{m,0})$ is for odd VSH and $(1 - \delta_{m,0})$ for even VSH. The orthogonality relations of the VSH can be further simplify by means of the recurrence relations of the spherical Bessel/Hankel functions [Eqs. (A.3) and (A.4)], which imply that

$$\left[\left(k \frac{\mathrm{d}z_\ell(kr)}{\mathrm{d}(kr)} \right)^2 + \ell(\ell + 1) \left(k \frac{z_\ell(kr)}{kr} \right)^2 \right] = k^2 \left[\ell z_{\ell-1}^2(kr) + \ell(\ell + 1) z_{\ell+1}^2(kr) \right], \tag{A.26}$$

$$\left[\left(\frac{z_\ell}{kr} \right)^2 + \left(\frac{1}{kr} \frac{\mathrm{d}[krz_\ell(kr)]}{\mathrm{d}(kr)} \right)^2 \right] = \ell(\ell + 1) \left[(\ell + 1) z_{\ell-1}^2(kr) + \ell z_{\ell+1}^2(kr) \right], \tag{A.27}$$

$$\left[\frac{z_\ell}{kr} \frac{\mathrm{d}z_\ell(kr)}{\mathrm{d}(kr)} + \left(\frac{1}{kr} \frac{\mathrm{d}[krz_\ell(kr)]}{\mathrm{d}(kr)} \right)^2 \right] = \ell(\ell + 1) \left[z_{\ell-1}^2(kr) - z_{\ell+1}^2(kr) \right]. \tag{A.28}$$

Size Corrected Dielectric Function

In this work, the optical properties of spherical gold (Au) nanoparticles (NPs) with radius $a = 12.5$ nm were studied. Even though the optical response of a non magnetic material is codified into the dielectric function $\varepsilon(\omega)$, the dielectric function for materials at the nanoscale differs from those in bulk due to surface effects. To perform a size correction to the dielectric function, let us decompose it into two additive contributions arising from intra- and interband electronic transitions [16]. If no spacial dispersion is considered, the intraband contribution of the dielectric function can be described by means of the Drude-Sommerfeld model

$$\frac{\varepsilon_{\mathrm{Drude}}(\omega)}{\varepsilon_0} = 1 - \frac{\omega_p^2}{\omega(\omega + i\gamma)}, \tag{B.1}$$

where ε_0 is the vacuum permittivity, and ω_p is the plasma frequency and γ the damping constant. In general, the damping constant is inversely proportional to the average time between collision events of the electrons inside the material and its value depends on the material itself and on its the geometry and dimensions. For example, the damping constant for a material in bulk γ^{Bulk} equals v_{F}/L with v_{F} the Fermi velocity and L the mean free path of the electrons. On the other hand, the damping constant γ_a^{NP} for a spherical NP of radius a deviates from γ^{Bulk} if the mean free path is greater than the size of the NP ($L > 2a$), in which case an effective mean free path replaces L, leading to the following expression for the damping constant:

$$\gamma_a^{\mathrm{NP}} = \gamma^{\mathrm{Bulk}} + A\frac{v_{\mathrm{F}}}{a}, \quad \text{with} \quad \gamma^{\mathrm{Bulk}} = \frac{v_{\mathrm{F}}}{L}, \tag{B.2}$$

where A is a theory dependent parameter whose exact value changes according to the approach employed to calculate the effective mean free path; for this work it is considered that $A = 1$.

In practice, the experimental data for the dielectric function of a material $\varepsilon_{\mathrm{Exp}}(\omega)$ corresponds to a material in bulk, so a size correction is performed on $\varepsilon_{\mathrm{Exp}}(\omega)$ if the optical properties of NPs are studied. The size correction is done by subtracting the intraband contribution that best fits the experimental bulk data and adding an intraband contribution considering Eq. (B.2), that is, the size corrected dielectric function $\varepsilon_{\mathrm{Size}}(\omega)$ is given by

$$\frac{\varepsilon_{\mathrm{Size}}(\omega)}{\varepsilon_0} = \frac{\varepsilon_{\mathrm{Exp}}(\omega)}{\varepsilon_0} + \left(-\frac{\varepsilon_{\mathrm{Drude}}(\omega)}{\varepsilon_0}\bigg|_{\gamma=\gamma^{\mathrm{Bulk}}} + \frac{\varepsilon_{\mathrm{Drude}}(\omega)}{\varepsilon_0}\bigg|_{\gamma=\gamma_a^{\mathrm{NP}}} \right), \tag{B.3}$$

The size correction in Eq. (B.3) considers the size effects on the intraband contribution of the dielectric function while the size corrections due to the interband contributions are neglected since it has been reported that they are relevant for NPs with radii smaller than 2 nm [19].

To employ the size corrected dielectric function [Eq. (B.3)], the parameters ω_p and γ^{Bulk} that best fit $\varepsilon_{\text{Exp}}(\omega)$ are needed. Let us develop two linear relations involving ω_p and γ^{Bulk} and the real and imaginary parts of $\varepsilon_{\text{Drude}}(\omega)$ following the method from Mendoza Herrera, Arboleda, Schinca, and Scaffardi. The real and imaginary parts of $\varepsilon_{\text{Drude}}(\omega)$ are

$$\text{Re}\left[\frac{\varepsilon_{\text{Drude}}(\omega)}{\varepsilon_0}\right] = 1 - \frac{\omega_p^2 \omega^2}{\omega^4 + (\omega\gamma)^2}, \quad \text{and} \quad \text{Im}\left[\frac{\varepsilon_{\text{Drude}}(\omega)}{\varepsilon_0}\right] = \frac{\omega_p^2(\omega\gamma)}{\omega^4 + (\omega\gamma)^2}. \tag{B.4}$$

according to Eq. (B.1). By multiplying the imaginary part of $\varepsilon_{\text{Drude}}(\omega)$ by ω and compairing it with its real part, one obtains that

$$\omega \, \text{Im}\left[\frac{\varepsilon_{\text{Drude}}(\omega)}{\varepsilon_0}\right] = \gamma\left(1 - \text{Re}\left[\frac{\varepsilon_{\text{Drude}}(\omega)}{\varepsilon_0}\right]\right), \tag{B.5}$$

and in a similar manner it can be verified that

$$\omega^2\left\{\text{Im}\left[\frac{\varepsilon_{\text{Drude}}(\omega)}{\varepsilon_0}\right]^2 + \left(1 - \text{Re}\left[\frac{\varepsilon_{\text{Drude}}(\omega)}{\varepsilon_0}\right]\right)^2\right\} = \omega_p^2\left(1 - \text{Re}\left[\frac{\varepsilon_{\text{Drude}}(\omega)}{\varepsilon_0}\right]\right). \tag{B.6}$$

By plotting the left hand side of Eqs. (B.5) and (B.6) as a function of $1 - \text{Re}[\varepsilon_{\text{Drude}}(\omega)/\varepsilon_0]$ and fitting two linear functions, the values for γ and ω_p^2 can be calculated according to the right hand side of Eqs. (B.5) and (B.6), respectively. As a final remark, the experimental dielectric
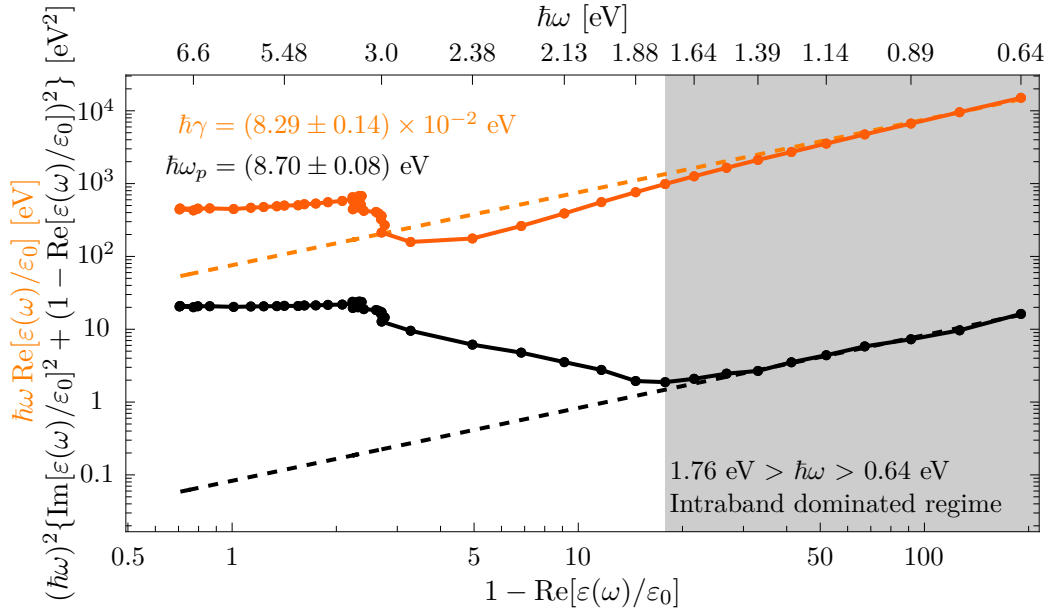
Fig. B.1: Plot of Eqs. (B.5) (orange) and (B.6) (black) evaluated with the experimental dielectric function reported by Johnson and Christy [15]. The shaded region corresponds to the frequency window from 0.64 eV to 1.76 eV, which is best described by the Drude-Sommerfeld model and which was considered to perform the linear fits (dashed), determinating a plasma frequency of $\hbar\omega_p = (8.70 \pm 0.08)$ eV and a damping constant of $\hbar\gamma = (8.29 \pm 0.14) \times 10^{-2}$ eV for Au.

function includes both an intra- and an interband contribution while Eqs. (B.5) and (B.6) are only valid for the intraband contribution of the dielectric function, thus the linear fits should be done within an spectral window into which the interband contributions are negligible compared to the Drude-Sommerfeld model, which best describes the optical properties of a material when $\omega \to 0$. The chose of the spectral window for the experimental data fit of the dielectric function can modify the calculated values of γ and ω_p.

In Fig. B.1, the left hand side of Eqs. (B.5) and (B.6) are plotted in orange and black, respectively, as a function of $1 - \text{Re}[\varepsilon(\omega)/\varepsilon_0]$, where $\varepsilon(\omega)$ corresponds to the experimental data of the dielectric function of Au (markers) reported by Johnson and Christy [15]; to ease the read of Fig. B.1, continuous lines between the data were added as a guide to the eye and the photon energy $\hbar\omega$ of selected points of the experimental data are shown on the top margin. The shaded region in Fig. B.1 is the frequency window 0.64 eV $< \hbar\omega < 1.76$ eV, into which the experimental data for Au shows a linear behavior as stated by Eqs.(B.5) and (B.6), that is, within this interval the intraband contribution to the dielectric function is dominant, thus the linear fits (dashed lines) where made with the data in this region, determinating a plasma frequency of $\hbar\omega_p = (8.70 \pm 0.08)$ eV and a damping constant of $\hbar\gamma = (8.29 \pm 0.14) \times 10^{-2}$ eV for Au in bulk. Once the plasma frequency and the damping constant for Au have been obtained, the size corrected dielectric for spheres can be calculated.

The real part (blue) and imaginary part (red) of the size corrected dielectric function for Au, based in the experimental data from Johnson and Christy, is plotted in Fig. B.2 as function of the photon energy $\hbar\omega$; on the top margin it is shown the convertion of the phton energy into wavlength λ. The size corrected dielectric function was calculated for several cases: Au in bulk
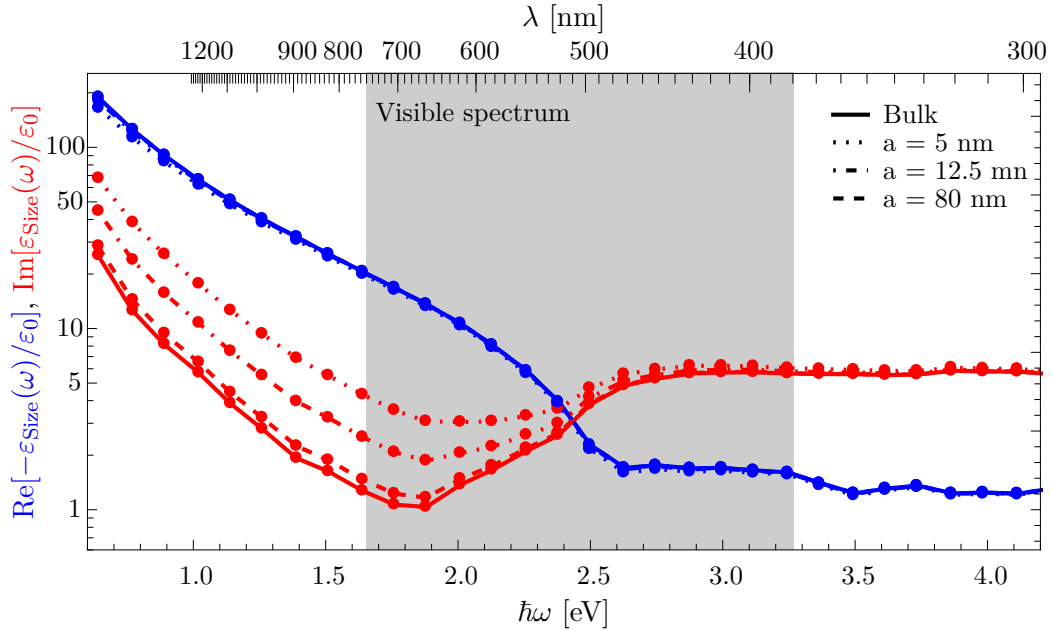
Fig. B.2: Real (blue) and imaginary (red) parts of the size corrected dielectric function of Au in bulk (continuous lines) and of spherical Au NPs of radius 5 nm (dotted lines), 12.5 nm (dash dotted lines) and 80 nm (dashed lines), as function of the photon energy $\hbar\omega$ (wavlength λ). The size corrected dielectric function was calculated from the experimental data of Johnson and Christy [15].

(continuous lines) and spherical Au NPs of radius 5 nm (dotted lines), 12.5 nm (dash dotted lines) and 80 nm (dashed lines); all lines are guides to the eye. The data in Fig. B.2 shows that the need for a size corrected dielectric functions increases as the frequency decreases (wavelength decreases), specifically for the visible spectrum (shaded region) the size correction is appreciated for $\hbar\omega < 2.5$ eV ($\lambda > 500$ nm). From Fig. B.2 it can also be seen that the imaginary part of the size corrected dielectric function differs the most from the bulk dielectric function compared to its real part, whose deflection from the bulk optical response are barely visible near $\hbar\omega \approx 1$ eV.

Bibliography

[1] R. S. Moirangthem, M. T. Yaseen, P.-K. Wei, J.-Y. Cheng, and Y.-C. Chang. Enhanced localized plasmonic detections using partially-embedded gold nanoparticles and ellipsometric measurements. *Biomedical Optics Express*, **3**(5):899, May 2012. ISSN: 2156-7085, 2156-7085. DOI: 10.1364/BOE.3.000899. URL: https://www.osapublishing.org/boe/abstract.cfm?uri=boe-3-5-899 (visited on 08/03/2021) (cited on page 3).

[2] G. Mie. Beiträge zur Optik trüber Medien, speziell kolloidaler Metallösungen. *Annalen der Physik*, **330**(3):377–445, 1908. ISSN: 00033804, 15213889. DOI: 10.1002/andp.19083300302. URL: http://doi.wiley.com/10.1002/andp.19083300302. Number: 3 (cited on page 3).

[3] H. Horvath. Gustav Mie and the scattering and absorption of light by particles: Historic developments and basics. *Journal of Quantitative Spectroscopy and Radiative Transfer*, **110**(11):787–799, July 2009. ISSN: 00224073. DOI: 10.1016/j.jqsrt.2009.02.022. URL: https://linkinghub.elsevier.com/retrieve/pii/S0022407309000715 (visited on 08/17/2020). Number: 11 (cited on page 3).

[4] C. F. Bohren and D. R. Huffman. *Absorption and Scattering of Light by Small Particles*. English. Wiley Science Paperbak Series. John Wiley & Sons, 1st edition, 1983. ISBN: 0-471-029340-7 (cited on pages 3, 5–8, 10–13, 17).

[5] L. Tsang, J. A. Kong, and K.-H. Ding. *Scattering of Electromagnetic Waves: Theories and Applications*. en. John Wiley & Sons, Inc., New York, USA, July 2000. ISBN: 978-0-471-22428-0 978-0-471-38799-2. DOI: 10.1002/0471224286. URL: http://doi.wiley.com/10.1002/0471224286 (visited on 05/17/2020) (cited on pages 3, 4, 6, 7).

[6] J. D. Jackson. *Classical electrodynamics*. Wiley, New York, 3rd ed edition, 1999. ISBN: 978-0-471-30932-1 (cited on page 6).

[7] M. Pellarin, C. Bonnet, J. Lermé, F. Perrier, J. Laverdant, M.-A. Lebeault, S. Hermelin, M. Hillenkamp, M. Broyer, and E. Cottancin. Forward and Backward Extinction Measurements on a Single Supported Nanoparticle: Implications of the Generalized Optical Theorem. *The Journal of Physical Chemistry C*, **123**(24):15217–15229, June 2019. ISSN: 1932-7447, 1932-7455. DOI: 10.1021/acs.jpcc.9b03245. URL: https://pubs.acs.org/doi/10.1021/acs.jpcc.9b03245 (visited on 08/03/2021) (cited on page 6).

[8] R. G. Newton. Optical theorem and beyond. en. *American Journal of Physics*, **44**(7):639–642, July 1976. ISSN: 0002-9505, 1943-2909. DOI: 10.1119/1.10324. URL: http://aapt.scitation.org/doi/10.1119/1.10324 (visited on 12/04/2020) (cited on pages 6, 7).

[9] A. V. Krasavin, P. Segovia, R. Dubrovka, N. Olivier, G. A. Wurtz, P. Ginzburg, and A. V. Zayats. Generalization of the optical theorem: experimental proof for radially polarized beams. en. *Light: Science & Applications*, **7**(1):36, Dec. 2018. ISSN: 2047-7538.

DOI: `10.1038/s41377-018-0025-x`. URL: `http://www.nature.com/articles/s41377-018-0025-x` (visited on 01/30/2021) (cited on page 7).

[10] E. W. Born Max. *Principle of Optics: Electromagnetic Theory of Propagation, Intergerence and Diffraction of Light.* Cambridge University Press, New York, USA, 7th edition, 1999. ISBN: 0-521-64222-1 (cited on page 7).

[11] A. Zangwill. *Modern Electrodynamics.* Cambridge University Press, Cambridge, 2013. ISBN: 978-0-521-89697-9 (cited on pages 7, 9).

[12] J. A. Stratton. *Electromagnetic theory.* McGraw-Hill, New York, 2012. ISBN: 978-1-4437-3054-9. URL: `https://archive.org/details/electromagnetict0000stra` (cited on pages 8, 10).

[13] R. G. Barrera, G. A. Estevez, and J Giraldo. Vector spherical harmonics and their application to magnetostatics. en. *European Journal of Physics*, **6**(4):287–294, Oct. 1985. ISSN: 0143-0807, 1361-6404. DOI: `10.1088/0143-0807/6/4/014`. URL: `https://iopscience.iop.org/article/10.1088/0143-0807/6/4/014` (visited on 09/17/2021) (cited on page 10).

[14] C. Maciel Escudero. *Linear Momentum Transfer from Swift Electrons to Small Metallic Nanoparticles: Dipole Approximation.* Master's thesis, UNAM, Mexico City, Mexico, 2017 (cited on page 16).

[15] P. B. Johnson and R. W. Christy. Optical Constants of the Noble Metals. *Physical Review B*, **6**(12):4370–4379, 1972. ISSN: 0556-2805. DOI: `10.1103/PhysRevB.6.4370`. URL: `https://link.aps.org/doi/10.1103/PhysRevB.6.4370` (visited on 05/30/2020) (cited on pages 16, 17, 19, 20, 38, 39).

[16] C. Noguez. Surface Plasmons on Metal Nanoparticles: The Influence of Shape and Physical Environment. *The Journal of Physical Chemistry C*, **111**(10):3806–3819, 2007. ISSN: 1932-7447, 1932-7455. DOI: `10.1021/jp066539m`. URL: `https://pubs.acs.org/doi/10.1021/jp066539m` (visited on 08/17/2020) (cited on pages 16, 37).

[17] H. Ibach and H. Lüth. *Solid-State Physics.* Springer Berlin Heidelberg, Berlin, Heidelberg, 2009. ISBN: 978-3-540-93803-3 978-3-540-93804-0. DOI: `10.1007/978-3-540-93804-0`. URL: `http://link.springer.com/10.1007/978-3-540-93804-0` (cited on page 19).

[18] G. B. Arfken and H.-J. Weber. *Mathematical methods for physicists.* Harcourt/Academic Press, San Diego, 5th ed edition, 2001. ISBN: 978-0-12-059825-0 (cited on page 34).

[19] L. J. Mendoza Herrera, D. M. Arboleda, D. C. Schinca, and L. B. Scaffardi. Determination of plasma frequency, damping constant, and size distribution from the complex dielectric function of noble metal nanoparticles. en. *Journal of Applied Physics*, **116**(23):233105, 2014. ISSN: 0021-8979, 1089-7550. DOI: `10.1063/1.4904349`. URL: `http://aip.scitation.org/doi/10.1063/1.4904349` (visited on 08/17/2020) (cited on page 38).

Index